FACILE GROWN OZONE OXIDE BASED PASSIVATION OF SILICON
FOR HIGH EFFICIENCY PHOTOVOLTAICS

by

Heidi Potts

A thesis submitted in conformity with the requirements
for the degree of Master of Science in Nanoscience at the University of Basel
The experimental work was carried out at the
Graduate Department of Electrical and Computer Engineering
University of Toronto

Abstract

Facile Grown Ozone Oxide Based Passivation of Silicon

for High Efficiency Photovoltaics

Heidi Potts

Master of Science in Nanoscience at the University of Basel

The experimental work was carried out at the

Graduate Department of Electrical and Computer Engineering

University of Toronto

2013

Surface passivation of crystalline silicon is extremely important for the design of ultra-thin high-efficiency photovoltaics. We introduce a novel passivation scheme based on ozone grown SiO_2 and plasma enhanced chemical vapour deposition SiN_x. An ozone oxidation chamber is designed for the growth of ultra-thin SiO_2 layers in a 1 % ozone in oxygen atmosphere at temperatures up to 450 °C. The chamber is calibrated and the ozone oxide growth is studied under varying conditions. This novel passivation scheme is analyzed in an extensive passivation study in order to find the optimal oxide growth conditions for surface passivation. The samples are characterized using spectroscopic ellipsometry, minority carrier lifetime measurement tools, parallel angle-resolved x-ray spectroscopy, and Fourier transform infrared spectroscopy. The results are further analyzed in the context of interfacial recombination models to infer interfacial defect and charge densities. A minority carrier lifetime of 1450 μs is reported for an n-type Czochralski silicon wafer with a 1.5 nm SiO_2 layer grown in ozone for 4 h at room temperature.

Acknowledgements

Contents

Nomenclature

μPCD .... Microwave photoconductance decay

a-Si .... Amorphous silicon

c-Si .... Crystalline silicon

ARXPS .... Angle resolved x-ray photoelectron spectroscopy

BACH .... Back Amorphous-Crystalline Silicon Heterojunction

CZ .... Czochralski

DB .... Dangling bond

ECD .... Excess carrier density

FT-IR .... Fourier transform infrared spectroscopy

FZ .... Float zone

HF .... Hydrogen fluoride

IR .... Infrared

LO .... Longitudinal optical

MEIS .... Medium energy ion spectroscopy

PCD .... Photoconductance decay

PECVD .... Plasma enhanced chemical vapour deposition

QSSPC .... Quasi steady state photoconductance

SE .... Spectroscopic ellipsometry

SiN$_x$ .... Amorphous silicon nitride

SiO$_2$ .... Silicon dioxide

SQ .... Shockley-Queisser

SRV .... Surface recombination velocity

TO .... Transverse optical

UofT .... University of Toronto

XPS .... X-ray photoelectron spectroscopy

List of Tables

List of Figures

Chapter 1

Introduction and Background

The first Chapter gives an introduction to the research topic. The importance of renewable energies is discussed and different photovoltaic technologies are presented. The design of ultra-thin crystalline silicon photovoltaics is explained and the concept of surface passivation is introduced. The chapter ends with a section on the research question and the thesis outline.

1.1 Motivation

Increasing energy consumption, limited fossil resources and increasing environmental cautiousness lead to a high demand for renewable energy sources. Providing new ways of energy production is not only a challenging task for the scientific community but it is also a hot topic in politics and society. Communities install solar panels on public buildings, countries provide financial support for green energy, and worldwide contracts like the Kyoto Protocol are signed in order to stem the consequences of climate change. Together with hydroelectric power and wind energy, solar energy is one of the important renewable energy sources. The global power consumption of 15 terawatts [1] is small compared to 174 petawatts [2] of solar radiation arriving on Earth in the upper atmosphere. Although solar energy is very abundant, we are still far away from using solar radiation to cover the global energy demand. Solar energy first needs to be converted into a more practical form of energy (e.g. into electricity by the use of photovoltaics) and then it must be transported and stored until it is being used. Each step is an on-going field of research.

1.2   Photovoltaics

For a long time, the potential of solar energy had not been recognized. In 1953 physicists at Bell Laboratories reported on the first silicon solar cell with an efficiency over 4 %. The first application of solar cells were in space, where solar cells were the only way of energy production, and high fabrication costs were not relevant. During the last decades, the potential of solar cells was recognized. The use of solar energy allows to overcome the dependency on natural resources and to reduce pollution was recognized. Photovoltaic research emerged as an important field which was highly encouraged and subsidized by different governments. Solar power is the available during high electricity consumption peaks. Most energy is consumed between noon and evening - a perfect match with the strongest solar radiation.

1.2.1   Photovoltaics for everyone

Energy resources are limited, energy prices increase, and pollution is a serious problem. But we are still burning coal. Photovoltaics and other renewable energy sources need to become cheap enough to be lower than the current electricity price, not only during peak hours (at noon), but on the daily average and without governmental subsidization. At the moment a price of $1/Watt at the module level (meaning that both the cell production and the installation costs are included) is the big goal for all solar technologies. This goal can be achieved by developing new long-lifetime devices with high efficiencies and low fabrication costs. Our research which will contribute to the development of high-efficiency low-cost silicon solar cells.

1.2.2   Principle of operation

Photovoltaics convert light directly to electricity. Electron-hole pairs are generated when a solar cell is exposed to radiation, provided that the photon energy is greater than the band gap of the absorber material. An internal potential difference (e.g. by a p-n junction in semiconductor photovoltaics) allows to separate the carriers within the cell. The motion of charges is called photocurrent. The charge carriers can be extracted and the electrical power can be used when a matching load is connected to the solar cell. A detailed explanation of the theory behind solar cells can be found in different books, e.g. *Solar Cells: Operating Principles, Technology, and System Applications* by M. A. Green [3]. In my project we focus on charge carrier recombination. A short introduction to recombination is given here and a more detailed explanation including a valid model for silicon surface recombination is given in Section 2.4.

1.2.3 Generation and recombination

In semiconductors, the valence band is almost completely occupied with electrons and the conduction band is almost empty. Electrons in the valence band are not mobile because there are no unoccupied states available to the moving electrons. Energy is needed for the transition of the electrons from the valence band to the conduction band. Charge carrier generation describes the process when electrons gain energy and make the transition into the conduction band. Two mobile charger carriers are created: the electron in the conduction band and a hole in the valence band. Charge carrier recombination is the process when an electron from the conduction band loses energy and recombines with a hole from the valence band, reducing the number of mobile charge carriers. In thermal equilibrium the generation rate and the recombination rate is equal, and the charger carrier density remains constant. During generation and recombination, an electron must gain or lose energy. The energy can be in form of photons or interactions with the lattice (phonons or other carriers). There are different recombination processes which can be distinguished by the underlying physical process: Band-to-band recombination (direct or indirect), trapping centre recombination (also known as Shockley-Read-Hall recombination), recombination involving excitons, and Auger recombination. A description of the recombination processes can be found in *Advanced Semiconductor Fundamentals* by R. F. Pierret [4]. Charge carrier recombination is an important loss mechanism in solar cells. In order to have a photocurrent, charger carriers must be generated, separated and extracted before they recombine. Recombination can be classified into bulk recombination and surface recombination because the material properties in bulk material are quite distinct from the properties at the surface. In solar cells it is an on-going challenge to minimize both bulk recombination and surface recombination. In ultra-thin technologies the surface recombinationis even more pronounced due to the high surface-to-volume ratio.

1.3 Photovoltaic technologies

Different photovoltaic devices are based on different materials and different technologies. The National Renewable Energy Laboratory (NREL) summarizes the achievement in photovoltaic technologies every year by updating their graph on photovoltaic efficiencies as shown in Figure 1.1. The different photovoltaic technologies are highlighted in different colors:

- Purple: Multi-junction devices. The highest efficiencies are achieved by combining several materials with different band gaps. However the fabrication of multi-junction devices is not easy due to problems like current-matching of the individual materials which are connected in series.

- Blue: Crystalline silicon devices. Crystalline silicon is the oldest photovoltaics material and still the most common technology. Over 80 % of the commercial solar cells are based on crystalline silicon. The abundance of silicon and the long-term stability are two major advantages.

- Green: Thin-film technologies. Flexible solar cells and other novel device properties can be achieved using thin-film technologies. Thin-film technologies are often based on non-standard materials or organics. The CIGS cell is a prominent example for flexible thin-film technologies.

- Red: Emerging photovoltaics. Dye-sensitized solar cells or quantum dot solar cells are examples for emerging photovoltaics. Until today their efficiency and their long-term stability is low, but recent development has shown major improvements with respect to the efficiency. Emerging photovoltaics are strong candidates because they can be produced using low-cost fabrication and materials.
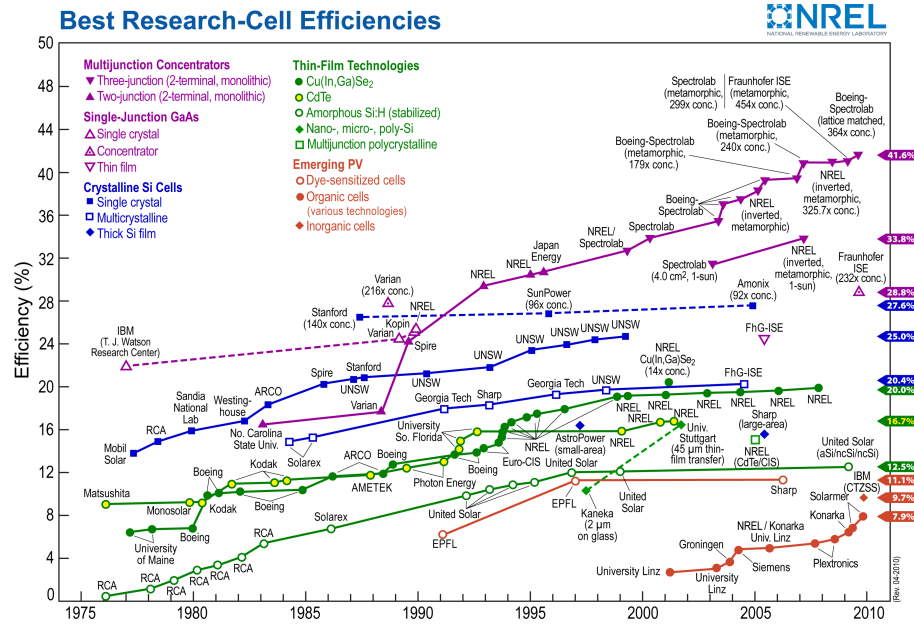
Figure 1.1: Record efficiencies for different solar cell technologies. The highest efficiencies are reached by multi-junction solar cells (purple).

1.3.1   Silicon photovoltaics

Silicon was the first material to be successfully used for solar cells. Silicon photovoltaics technology has evolved over more than 50 years, and until today, the market is dominated by silicon photovoltaics due to several advantages. Besides low production cost and high efficiency, the long-term stability is an extremely important point. Solar cells are constantly exposed to solar radiation. The high intensity radiation of the sun causes damage to materials. The damage strongly depends on the type of material.

It has been shown [5] that silicon solar cells still retain most of their efficiency (meaning there is very low damage) after many years of operation, whereas other technologies degrade much faster. The high long-term stability is a huge advantage for solar cells which should operate for a long time in order to keep the maintenance costs low.

(a) Silicon band structure [6]   (b) Solar radiation spectrum [7]
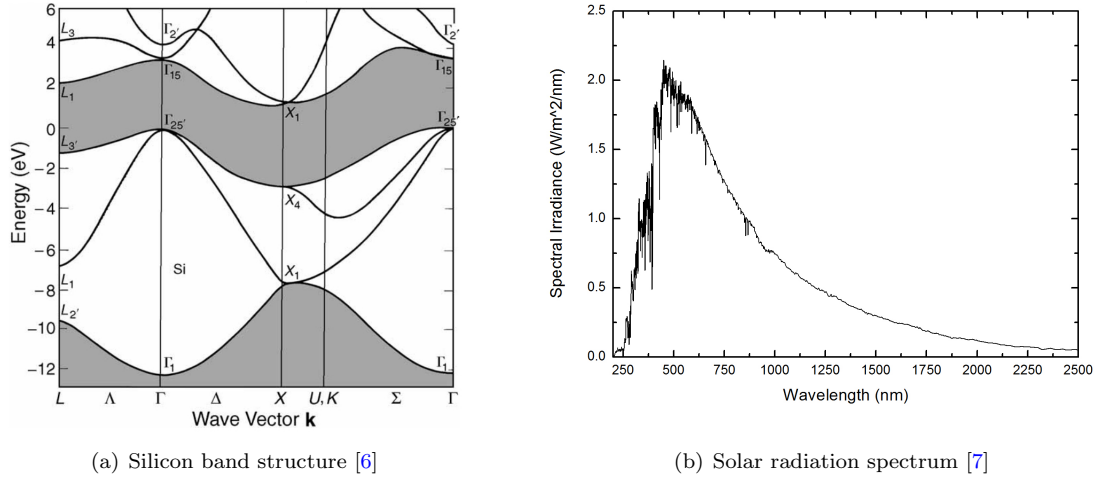
Figure 1.2: a) Silicon band structure. The forbidden energy band is shown in dark grey. b) Solar radiation spectrum. The optimal band gap for a single junction solar cell can be calculated from the solar radiation spectrum. The optimal band gap is 1.1 eV which corresponds to the band gap of silicon.

Figure 1.2(a) shows the band structure for silicon. The allowed energy states are shown in white and the forbidden energy band is shown in dark grey. The band gap is the difference in energy between the maximal-energy state in the valence band and the minimal-energy state in the conduction band. Crystalline silicon has band gap of 1.1 eV at 300 K. It is an indirect band gap, meaning that the k-vector of the minimal-energy state and the k-vector of the maximal-energy state are different. In order to shift an electron to the conduction band, a phonon is needed which enables the change in k-vector (momentum). This has an important effect on the design of solar cells. Indirect band gap materials do not absorb light very well, and thus the absorption layer must be thicker. From an energy point of view, the band gap of silicon is close to optimal band gap for a single-junction solar cell. The radiation spectrum of the sun is shown in Figure 1.2(b). Only photons which carry more energy than the band gap can be absorbed by a material. If the band gap is very high, most photons of the sunlight cannot be absorbed. If the band gap is very low, lots of photons are absorbed but most of their energy is lost. The optimum band gap for a solar cell material is a compromise between high current (low band gap) and high voltage (high band gap). Under solar radiation, the optimum band gap is 1.1 eV for a single-junction solar cell.

1.3.2 Efficiency of solar cells

The maximum theoretical efficiency of a solar cell using a p-n junction with a band gap of 1.1 eV is about 30 %. The theoretical limit is based on the assumption that the solar spectrum consists of photons with various energies conforming to a 5600 K blackbody radiation distribution filtered by the Earth's atmosphere. The calculation of the theoretical limit was first done by Shockley and Queisser [8] and is therefore known as Shockley-Queisser (SQ) limit. It's an on-going challenge to increase the efficiency of solar cells. The efficiency of all existing solar cell technologies is compared by M. A. Green and a group of authors from different solar cell laboratories in the world in the publication *Solar Cell Efficiency Tables* [9] every 6 months. In 2012, the efficiency record for single junction solar cells was held by GaAs thin film cells with an efficiency of 28 % [9], followed by crystalline silicon (c-Si) with an efficiency of 25 % [10]. Solar cell efficiencies exceeding the SQ limit can be achieved by designing multi-junction solar cells. A multi-junction cell consists of several light absorbing layers with different band gaps. This allows to completely use the energy of high energy photons, without wasting the energy of low energy photons. In principle, many different band gap materials can be stacked in order to form one high-efficiency device. The stack of cells is connected in series which creates the need of current matching. The realization of multi-junction solar cells is therefore not straight forward and makes them not applicable for commercial production. Further efficiency improvements can be achieved by the use of concentrating lenses or mirrors that focus light on smaller cells.

1.3.3 Cost Considerations

Facile production, reduced material costs, and low thermal budget is desired, due to the increasing costs for labour, material and energy. Although their efficiency is only in the mid-range, crystalline silicon solar cells are a strong candidate to meet the requirement for cheap energy production. In a study on crystalline silicon photovoltaics by Upadhyaya *et al*, material cost accounted for over 50 % of the total module cost as shown in Figure 1.3. The wafer cost is highly dependent on the energy price and the study should therefore be regarded as a trend and not as exact values. The results of the cost analysis indicate that reduction of material costs constitutes an important avenue towards low-cost energy production using solar cells. There are two main approaches in order to reduce the material cost of silicon photovoltaics:

1. the design of thin-film silicon solar cells based low-cost amorphous silicon a-Si:H

2. the reduction of the present day wafer thickness which is $\sim$200 μm

The overall fabrication cost is reduced by using facile low temperature processes. In our research we focus on the design of ultra-thin low-temperature crystalline silicon devices.
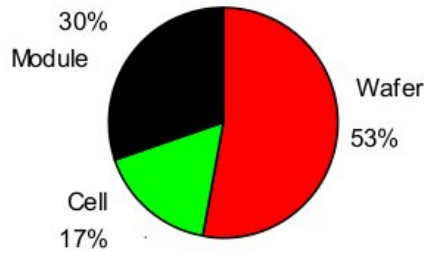
Figure 1.3: Solar module cost calculation for silicon photovoltaics in 2006 [11]. Material costs account for over 50 % of the total cost of an installed solar device. This result indicates the importance of thickness reduction on the way towards low-cost energy production.

1.4 Ultra-thin silicon photovoltaic devices

The increasing price for materials drives the research towards ultra-thin technologies. While reducing the size towards ultra-thin solar cells, the criterion of high efficiency has to be met at the same time. New device designs are needed for ultra-thin high-efficiency silicon photovoltaics. The development of new device structures is an important field of research in our group at the University of Toronto. The Back Amorphous-Crystalline Silicon Heterojunction (BACH) photovoltaic device is one example of a novel solar cell design, which has received considerable attention due to its excellent efficiency, while using all low-temperature fabrication methods. The BACH cell structure is shown in Figure 1.4. It consists of an n-type c-Si absorber layer and differently doped amorphous silicon (a-Si) layers. A p-type a-Si layer forms the p-n junction, while a n-type a-Si layer forms an iso-junction which helps to collect the charge carriers by inducing band bending. All contacts are on the back of the cell which reduces the optical losses. A novel bilayer passivation scheme, which consists of native oxide (1 nm) and PECVD SiN$_x$, is used for surface passivation. Parasitic optical losses are avoided due to the low absorption by the passivation layers. Chowdhury et al have reported an efficiency of 16.7 % under AM1.5 solar radiation spectrum. This is an excellent efficiency for untextured silicon and unconcentrated light. Ultra-thin crystalline silicon is not optimal from a light absorption perspective because it is an indirect band-gap semiconductor. However, absorption only becomes a problem for a thickness below 100 μm. In this regime, additional light trapping structures can be used to ensure optimal light absorption. Additional light trapping structures and structuring of the surface will allow the BACH cell design to reach even higher efficiencies and to further reduce the thickness of the absorber layer.
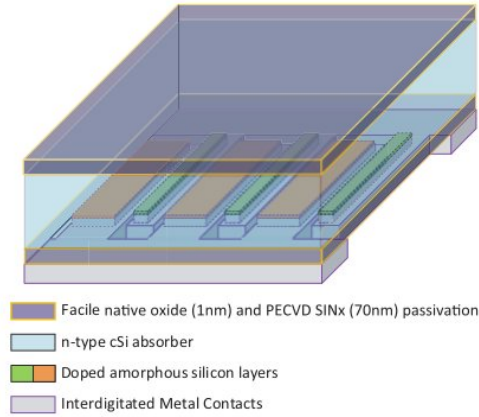
Figure 1.4: BACH cell schematic by Chowdhury *et al.* The cell is based on an ultra-thin crystalline silicon wafer with facile oxide surface passivation. Optical losses are avoided by placing all contacts on the back of the solar cell. An efficiency of 16.7 % was reported for untextured silicon.

1.4.1 Surface passivation

In order to design high-efficiency solar cells, all loss mechanisms in a solar cells must be reduced. Charge carrier recombination is one very important loss mechanism. It can occur both in bulk material and on the surface. Charge carrier recombination at the surface becomes more pronounced when reducing the wafer thickness. Surface recombination can be reduced by passivation of the surfaces. Finding appropriate passivation layers, which reduce surface recombination but do not disturb the charge carrier generation and extraction, is a key challenge for ultra-thin high-efficiency photovoltaics. There are different approaches for surface passivation, and different methods are needed for different materials and solar cells technologies. Unpassivated crystalline silicon shows a high surface recombination rate due to a high density of unsaturated bonds at the surface (also known as dangling bonds). The passivation effect of additional passivation layers can be attributed to two different effects:

1. the defect density is reduced by saturation of dangling bonds

2. the minority carriers are repelled from the surface by a local electric field

Surface passivation will be discussed in detail in Section 2.2. Thermal silicon oxide is the standard surface passivation scheme in industrial processes. However, there are other passivation schemes which are more suitable for the design of ultra-thin silicon photovoltaic devices. In the BACH cell, a bilayer passivation scheme using native SiO_2 and PECVD SiN_x was used to achieve excellent surface passivation. The native SiO_2 and PECVD SiN_x passivation scheme is the basis for the novel ozone oxide based passivation scheme which is introduced in this project.

1.5   Research question

The research of this project aims to contribute to the design of low-thermal-budget high-efficiency ultra-thin silicon photovoltaics. The focus lies on surface passivation of crystalline silicon. A novel bilayer passivation scheme using ozone grown SiO_2 and PECVD silicon nitride is analyzed in detail. First the chamber for oxidation using ozone as oxidant is designed and calibrated. Well-defined oxide layers with controllable oxide thickness (<5 nm) can be grown by adjusting parameters like the oxidation time and the oxidation temperature. Silicon nitride is then deposited on top of the oxide, and minority carrier life time is measured. An extensive study is carried out relating the oxide thickness and the oxidation temperature to the quality of surface passivation. The influence of other parameters, e.g. ozone concentration and doping of silicon, are considered in additional experiments.

1.5.1   Research methodology

The ozone oxidation chamber is designed according to our requirements and fabricated by the machine shop at the UofT. An ozone generator is purchased and attached to the chamber. The gas flow of ozone containing oxygen can be adjusted and other gases may be introduced into the chamber if desired. The heating system with a temperature controller is designed to allow heating of the sample up to 450 °C. The chamber is completely sealed to avoid danger by ozone leakage. The gas from the outlet of the chamber passes through an ozone destructor before it can be released into the air. The temperature inside the chamber is analyzed and the position of our samples is calibrated. After setup and calibration of the chamber, samples are grown under varying conditions, and then characterized by different methods. The oxide thickness is measured using ellipsometry and angle-resolved x-ray spectroscopy. The surface passivation is analyzed by measuring minority carrier lifetimes using microwave photoconductance decay (μPCD) and quasistatic photoconductance decay (QSSPC). Fourier-transform infrared absorption spectroscopy (FT-IR) is used to characterize the Si/SiO_2 interface quality of the ozone grown silicon oxide.

1.6   Thesis outline

My thesis is divided into the following chapters:

Chapter 1: Introduction

In the first chapter the concept of solar energy is introduced. The basic physics behind solar cells and the principle of charge carrier generation and recombination is summarized.

Chapter 2: Theory

The theory behind this project is explained in the second chapter. Different oxidation methods for crystalline silicon are described in the first section. The theory of surface passivation is explained, and different passivation schemes are reviewed. The measurement techniques for carrier lifetimes are introduced, and the dangling bond recombination theory is explained. Finally, the theory of thin-film thickness measurement techniques is presented.

Chapter 3: Materials and Methods

The third chapter presents the materials and tools which are used in this project. The data analysis for different measurement techniques is explained using illustrative example measurements. The main experimental studies are presented in the last section.

Chapter 4: Results and Discussion

Chapter 4 presents the results of the experimental work as well as a critical discussion. The three main results of this thesis are: 1) The setup and calibration of our custom-built ozone oxidation chamber. 2) The characterization of the ozone oxide growth. 3) An extensive study of the surface passivation quality for our novel bilayer surface passivation scheme based on ultra-thin ozone-SiO_2 and PECVD-SiN_x.

Chapter 5: Conclusion and Outlook

A summary of my work and an outlook for future experiments is given in the last chapter.

Appendix

Additional information on the oxidation chamber is given in the Appendix. A user manual for the oxidation chamber is provided, and additional experimental results are presented. The theoretical background of the FT-IR characterization is explained, and the literature on silicon oxidation by ozone is reviewed, emphasizing the advantages of ozone oxidation.

Chapter 2

Theory

The theory behind our research is presented in this chapter. The fabrication and the properties of silicon oxide are summarized. Surface passivation is discussed in detail and the surface recombination velocity is introduced. Surface passivation layers are further discussed in the context of anti-reflection coatings. The theory behind carrier lifetime measurement devices is explained. The dangling bond recombination model is introduced and the calculation of interface parameters is presented. The theory of spectroscopic ellipsometry and x-ray photoelectron spectroscopy is described in the context of thickness measurements of ultra-thin silicon oxide films.

2.1 Silicon oxide

Silicon (Si) is the most used semiconductor material for microelectronic devices. One of the main advantages is the possibility to grow an insulating silicon oxide (SiO_2) layer directly on the substrate. Miniaturization of electronic devices increases the demand on material properties. The silicon oxide structure and the Si/SiO_2 interface become important when down-scaling electronic devices. At the interface, compositional and structural transition layers are formed. The material properties of those transition layers differ from Si or SiO_2 bulk material. The standard technology for SiO_2 fabrication is thermal oxidation where the sample is exposed to oxygen (O_2) at high temperatures (usually higher than 800 °C). Fast oxide growth is achieved with thermal oxidation, but it's not a favourable process for photovoltaic applications because high temperatures increase the energy consumption and therefore the thermal budget. Furthermore, high temperature steps are likely to induce material degradation, especially when using low solar grade silicon materials such as Czochralski silicon or poly-crystalline silicon (which is commonly used in the PV industry). The material degradation occurs due to thermal

stress or dopant migration. Therefore, the use of low-temperature oxidation processes instead of thermal oxidation is desired for photovoltaics applications.

2.1.1 Facile oxide

The term facile oxide has been introduced by our group. It is used to describe all thin silicon oxides which can be grown at low temperatures, as opposed to thermal oxide which requires temperatures greater than 800 °C. Specifically we distinguish between:

- facile native oxide

- facile chemical oxide

- facile ozone oxide

The use of facile oxide is an important step towards low-cost high-efficiency photovoltaic devices. It enables to use of low-quality silicon such as Czochralski (CZ) silicon and poly-crystalline silicon, which are not suitable for high temperature processing because of the material degradation caused by high temperature cycling. The use of facile oxide facilitates the device production and reduces the thermal budget when compared to thermal oxide.

Native oxide

When pure silicon is stored under atmospheric conditions a native oxide layer starts to grow immediately. The native oxide growth is fast in the beginning and slows down after the first couple of days. The native oxide layer saturates at about 10 Å thickness after 4 weeks of oxidation under atmospheric conditions.

Chemical oxide

Thin silicon oxide films can be grown using chemical oxidation methods. Oxidation in hot deionized water or and oxidation in a hot diluted hydrochloric acid (HCl) has been used for passivation purposes by other groups [12].

Ozone oxide

Ozone oxidation, which has been first reported in 1989 [13], exhibits several advantages compared to other oxidation methods: it is more environmentally friendly than other oxidizing species (e.g. N_2O), it can be generated in high concentrations, and there are no highly energetic particles which would cause damage to the sample. Depending on the ozone concentration and the temperature, oxide layers

of 50 nm and thicker can be grown. From a quality point of view, the ozone induced SiO_2 shows advantages compared to other oxidation techniques. One advantage which has been reported by several groups is the high Si/SiO_2 interface quality as explained in the following section. A detailed description of silicon oxidation by ozone can be found in the Appendix D. It includes an overview over various types of ozone generators, the oxide growth rate, the advantages of ozone oxidation compared to thermal oxidation, and molecular dynamics simulations of the oxide growth.

2.1.2 Silicon/silicon oxide interface

The Si/SiO_2 interface is extremely important for device fabrication and is a fascinating subject which is still not completely understood. There are two kinds of transition layers at the Si/SiO_2 interface: the compositional and the structural transition layer. The compositional transition layer consists of intermediate oxidation states of silicon. There are Si^{1+}, Si^{2+} and Si^{3+} sub-oxides between the SiO_2 and the bulk silicon. The compositional layer is usually restricted to one or two atomic layers. The structural transition layer takes place gradually in a wide region. It is due to the extension of the SiO_2 lattice with respect to the silicon lattice. On the Si side of the interface, it has been shown that the structural transition layer is usually two atomic layers thick [14]. On the SiO_2 side of the interface, the structural transition layer is considered to be approximately 1 nm thick. A detailed discussion of the transition layers can be found in [15] and references therein. There are several methods to analyze the nature of the Si/SiO_2 transition layer: The structural transition layer can be shown by a change of the etching rate of SiO_2 near the interface. The interface of ultrathin SiO_2 films can be studied using photoelectron spectroscopy (XPS), fourier transform infrared spectroscopy (FT-IR) and medium energy ion spectroscopy (MEIS). The results of different characterization methods are summarized in the Appendix D.3. We consider the Si/SiO_2 interface quality to be an important parameter when using SiO_2 for surface passivation. Transition layers can be related to defects which act as recombination centers. We use FT-IR to characterize our samples. The details are discussed in the Appendix C.

2.2 Surface passivation

Different passivation schemes can be used to prevent carrier recombination at the surface. The surface passivation quality cannot be measured directly. It is convenient to measure the effective minority carrier lifetime and then calculate the surface recombination velocity (SRV). The SRV is nearly independent of sample parameters and can be used as a measure for surface passivation quality.

2.2.1   Surface recombination velocity

The effective lifetime of the minority carriers τ_{eff} can be measured directly using lifetime measurement tools. It is given by

$$\frac{1}{\tau_{eff}} = \frac{1}{\tau_{surface}} + \frac{1}{\tau_{bulk}} \tag{2.1}$$

where $\tau_{surface}$ and τ_{bulk} are the lifetimes due to surface and bulk recombination respectively. The measured lifetime depends on the passivation quality and a few sample parameters i.e. thickness and resistivity of the sample. In order to compare the surface passivation quality of different samples, the surface recombination velocity can be evaluated. The effective surface recombination velocity S_{eff} is related to the effective lifetime by

$$\frac{1}{\tau_{eff}} = \frac{1}{\tau_{bulk}} + \frac{2S_{eff}}{w} \tag{2.2}$$

where w is the wafer thickness [16]. The effective surface recombination velocity is normalized by the thickness of the sample and is therefore a good measure to compare the surface passivation of different samples. We usually assume infinite bulk lifetime which simplifies Equation 2.2 to

$$S_{eff} = \frac{w}{2\tau_{eff}} \tag{2.3}$$

Two common ways of measuring effective carrier lifetimes are transient photoconductance decay (PCD) and quasi-steady-state photoconductance (QSSPC) and will be described in more detail in Section 2.3.

2.2.2   Surface passivation of crystalline silicon

In my project, we focus on the passivation of crystalline silicon (c-Si). At the surface of crystalline silicon, the crystal symmetry is disturbed which leads to the existence of unsaturated bonds. The unsaturated bonds (also known as dangling bonds) are defects which act as recombination centres. Surface passivation is needed in order to minimize recombination due to dangling bonds at the surface. Surface passivation can be achieved by a) minimizing the recombination centre density or b) reducing the density of the minority carriers at the surface. When comparing different passivation schemes there are two items which have to be considered:

1. The surface recombination velocity does not only depend on the surface passivation but also on the resistivity and the material quality of the sample. It is much easier to obtain low surface recombination velocities for high-resistivity FZ silicon than for low-resistivity CZ silicon. This makes it difficult to compare individual results.

2. Even the best surface passivation may not be suitable for photovoltaic applications if the surface reflection is high. A high surface reflectivity reduces the current density because less light is absorbed.
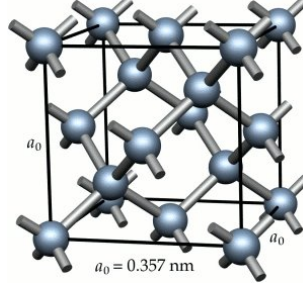
Figure 2.1: Crystal structure of silicon. Silicon crystallizes in the diamond structure. At the surface, the symmetry of a silicon crystal is disturbed which leads to the existence of unsaturated bonds.

Review of common surface passivation schemes

The standard passivation scheme in industrial solar cell fabrication is a thin layer of thermally grown silicon oxide. However, the growth of thermal SiO_2 requires high temperature processing ($> 800\ ^\circ C$) which makes it unsuitable for the use of lower quality ultra-thin silicon substrates (due to thermal stress and dopant migration). Furthermore, the high temperature cycle also increases the thermal budget of the fabrication. Different low-temperature surface passivation schemes are currently investigated in order to replace the high-temperature thermal SiO_2 passivation. They include amorphous silicon (a-Si:H) [17], Al_2O_3 films deposited by atomic layer deposition [18], amorphous silicon carbide (SiC_x) [19], and PECVD amorphous SiN_x [16]. These passivation schemes result in effective surface recombination velocities in the order of 5-20 cm/s. We want to focus on amorphous SiN_x which is easy to fabricate and gives good surface passivation. In SiN_x films, the surface passivation is achieved by a combination of two effects: 1) During fabrication, hydrogen from the precursor gases SiH_4 and NH_3 diffuses to the c-Si surface and passivates the defects at the interface, and 2) fixed positive charges at the c-Si/SiN_x interface lead to field effect passivation [20]. However, an induced inversion layer due to the high trapped charge density leads to parasitic shunting which reduces the short circuit current [21]. An additional thin layer of silicon oxide between the c-Si and the SiN_x can be used in order to remove or reduce the parasitic shunting effect. Recently, very effective surface passivation has been reported using plasma deposited SiO_x/a-SiN_x:H stacks [22]. However the plasma deposited silicon oxide layers are rather thick (in the range of 50 nm) and therefore the refractive index gradient of the stack is not favourable for light trapping. An alternative passivation scheme with a thinner oxide layer consists of stacks of thermal-SiO_2 and

plasma-enhanced chemical vapour deposition (PECVD)-SiN$_x$ [23, 24, 25]. The reported effective surface recombination velocity is excellent (2.4 cm/s) but the fabrication is complex, and high temperatures (800 °C) are needed for thermally grown silicon oxide. A new way of oxidation is desired in order to replace the thermal silicon oxidation. In this project we study low-temperature ozone oxide growth, and introduce a novel all low-temperature fabrication scheme for SiO$_2$/SiN$_x$ bilayer passivation.

2.2.3 Novel surface passivation schemes

A novel surface passivation scheme was recently proposed by our group. It is based on ultra-thin SiO$_2$ and PECVD-SiN$_x$. Chowdhury *et al* recently reported on excellent surface passivation using a bilayer of native SiO$_2$ and SiN$_x$. An effective surface recombination velocity of 8 cm/s [26] was measured. Figure 2.2(a) shows that the passivation quality increases with the native oxide thickness. The drawback of facile native oxide is the growth time of 28 days for 10 Å of SiO$_2$. The oxide thickness saturates at approximately 10 Å and thicker oxides cannot be grown. A second novel passivation scheme is proposed in this project. It is based on the same materials, but the native-SiO$_2$ is replaced by ozone-SiO$_2$. We study the surface passivation of an ultra-thin layer (< 5 nm) of ozone-SiO$_2$ and a thin layer (90 nm) of PECVD-SiN$_x$. A schematic of the passivation scheme is shown in Figure 2.2(b). Ozone induced oxidation has been reported to enable fast silicon oxide growth at low temperatures [27], with a high-quality Si/SiO$_2$ interface [28, 29]. Furthermore, ozone allows to grow thicker oxides which seems to be favourable for surface passivation according to Chowdhury's results. We conclude that ozone SiO$_2$ is considered an interesting approach for surface passivation.
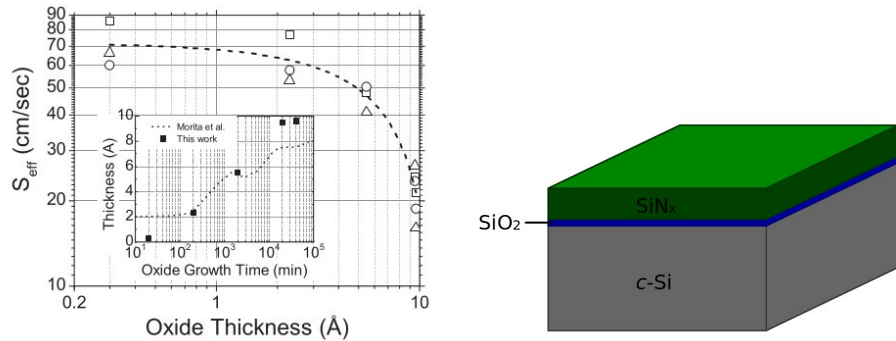
(a) Resutls of native-SiO$_2$/PECVD-SiN$_x$ [26]   (b) Schematic of ozone-SiO$_2$/PECVD-SiN$_x$

Figure 2.2: Novel bilayer passivation schemes. a) Surface passivation by native oxide and silicon nitride. The passivation quality increases with the oxide thickness. b) Schematic: an ultra-thin layer (< 5 nm) of ozone-SiO$_2$ and a thin layer (90 nm) of PECVD-SiN$_x$ are grown and deposited on crystalline silicon.

2.2.4 Surface reflectivity

When designing passivation schemes for solar cells, the surface reflectivity has to be considered. The best solar cell design with excellent surface passivation cannot yield high efficiencies, if the light is reflected at the surface instead of being absorbed by the absorption layer. The refractive index gradient of the passivation layers is a good indicator for surface reflectivity. An increase of refractive index is desired to avoid the losses due to back reflection. The refractive index of SiN_x is usually on the order of 2.0 at 630 nm. The exact value is largely dependent on the deposition conditions [30]. A bilayer of SiN_x ($n = 2$) and SiO_2 ($n = 1.5$) on c-Si ($n = 3.4$) is therefore not optimal from a anti-reflection coating point of view. The losses can be minimized if the thickness of the SiO_2 is only a few nm thin. A more precise analysis can be obtained by calculating the surface reflectivity in dependence on the layer thicknesses and the refractive indices. The surface reflection can be calculated using the double layer reflection matrix which is similar to a Fabry-Perot calculation. The derivation can be found in a calculation by Moys *et al* [31] and will be summarized here. The reflected energy is given by

$$R = rr* \tag{2.4}$$

where r is the amplitude reflectance which is given by

$$r = \frac{n_0 C_1 - n_3 C_4 + i(n_0 n_0 C_2 - C_3)}{n_0 C_1 + n_3 C_4 + i(n_0 n_0 C_2 + C_3)} \tag{2.5}$$

where C_1, C_2, C_3, C_4 are the elements of the characteristic Matrix M of the double layer. The characteristic matrix is given by

$$M = \begin{bmatrix} C_1 & iC_2 \\ iC_3 & C_4 \end{bmatrix} \tag{2.6}$$

The matrix elements can be written in terms of $\Phi_r = 2\Pi n_r d_r / \lambda$

$$C_1 = \cos\Phi_1 \cos\Phi_2 - (n_2/n_1)\sin\Phi_1 \sin\Phi_2 \tag{2.7}$$

$$C_2 = (1/n_2)\cos\Phi_1 \sin\Phi_2 + (1/n_1)\sin\Phi_1 \cos\Phi_2 \tag{2.8}$$

$$C_3 = n_2 \cos\Phi_1 \sin\Phi_2 + n_1 \sin\Phi_1 \cos\Phi_2 \tag{2.9}$$

$$C_4 = \cos\Phi_1 \cos\Phi_2 - (n_1/n_2)\sin\Phi_1 \sin\Phi_2 \tag{2.10}$$

Here n_r and d_r are the refractive index and the thickness of the layers, r being 1 for the outer layer (SiN_x) and 2 for the inner layer (SiO_2). The reflectance is given by

$$R = \frac{X - 2}{X + 2} \tag{2.11}$$

where

$$X = \frac{n_0}{n_3}C_1^2 + n_0 n_3 C_2^2 + \frac{1}{n_0 n_3}C_3^2 + \frac{n_3}{n_0}C_4^2 \tag{2.12}$$

Here, the refractive indices n_0 for the surrounding material (air), and n_3 and for the substrate (Si) have been introduced. The above equations are used in this project to calculate the reflected energy in dependence on the layer thickness and the wavelength. The total reflected energy R_{tot} of the surface under AM1.5 illumination can be obtained by integration over the solar radiation spectrum

$$R_{tot} = \frac{\int \frac{R(\lambda)SI(\lambda)}{E(\lambda)}d\lambda}{\int \frac{SI(\lambda)}{E(\lambda)}d\lambda} \tag{2.13}$$

where $SI(\lambda)$ is the spectral irradiance at AM1.5 and $E(\lambda)$ is the photon energy. In our calculations the spectrum by Wehrli *et al* [7] is used. The integration is done between a wavelength of 300 nm and 1200 nm and a $d\lambda$ of 1 nm. The denominator describes the total photon flux and can be calculated to be 3.60E21 photons/(s·m^2) which is in agreement with literature values.

2.3 Measurement of carrier lifetimes

The concentration of free charge carriers (electron-hole pairs) in a semiconductor depends on the material, the dopant concentration, and the temperature. An excess of electron-hole pairs Δn is created under illumination, if the photon energy is greater than the band gap of the material. The excess carrier concentration decays due to recombination processes

$$\Delta n(t) = \Delta n(0)e^{-t/\tau} \tag{2.14}$$

where τ is the carrier lifetime, and Δn(0) is the excess carrier concentration at time t=0. The carrier lifetime τ can be calculated by

$$\frac{1}{\tau} = \frac{1}{\tau_1} + \frac{1}{\tau_2} + ... \tag{2.15}$$

When different recombination mechanisms with different lifetimes τ_1, τ_2 etc are involved [32]. For solar cells, long carrier lifetimes are important because charge carriers must be extracted in order to generate

a photo-current. We are particularly interested in the minority carrier lifetimes because those are the limiting carrier for the electrical current. The carrier lifetimes also depends on the number of injected excess carriers which is why we measure the excess carrier density (ECD) dependent minority carrier lifetime. In order to measure the carrier lifetime, the sample is illuminated with a short light pulse. The decay of excess carrier density is then measured after the illumination is turned off. The excess carrier density is measured either by inductive coupling or by microwave reflection. Both methods are contact-less detection methods. The measured value is an average value across the sample. A sample with low bulk recombination (i.e. a high resistivity wafer) should be chosen to ensure that the measured lifetimes is mostly characterized by the surface lifetime. Two methods are commonly used to measure carrier lifetimes: transient photoconductance decay (PCD) and quasi steady state photoconductance (QSSPC). The two methods differ by the illumination duration. QSSPC is more accurate for low carrier lifetimes and is usually used to measure samples where the lifetime is expected to be below 200 μs. In our lab we compare the lifetime data from two devices: The Semilab WT-2000 is based on a microwave detected transient photoconductance decay measurement and is referred to as μPCD. The Sinton WCT-120 measures the carrier density by inductive coupling and has both a transient and a quasi-steady state measurement mode.

2.3.1   Photoconductance decay (PCD)

Photoconductance decay is based on analyzing photoconductance decay transients after a short light pulse from a laser or a flash lamp. The effective lifetime τ is obtained from the slope of the decay curve

$$\tau_{eff} = \frac{\Delta n}{d(\Delta n)/dt} \tag{2.16}$$

where Δn is the minority carrier concentration. The minority carrier concentration is directly related to the signal of microwave reflectance or the pickup coil. The transient photoconductance decay method is accurate for samples with long carrier lifetimes. However for effective lifetimes shorter than 50 μs surface recombination transients and minority-carrier spreading complicate the interpretation of the measurement results [33].

2.3.2   Quasi-steady-state photoconductance (QSSPC)

Quasi-steady-state photoconductance (QSSPC) is usually used for samples with lifetimes lower than 200 μs. Generation and recombination of electron-hole pairs is balanced under steady-state illumination. The photogenerated excess electron and hole densities result in an increase in the conductance of the

sample. The excess photoconductance σ_L in dependance of the average excess minority carrier density Δn_{avg} is given by

$$\sigma_L = q\Delta n_{avg}(\mu_n + \mu_p)w \tag{2.17}$$

where q is the carrier charge, μ_n and μ_p are the electron an hole mobilities respectively, and w is the thickness of the sample. The effective minority carrier lifetime can be determined from

$$\tau_{eff} = \frac{\sigma_L}{J_{ph}(\mu_n + \mu_p)} \tag{2.18}$$

where J_{Ph} is the photogenerated current density which can be found in lookup tables for different silicon samples [33]. In the steady-state approach a light pulse is used which varies very slowly compared to the effective lifetime of the sample. Compared to a transient decay approach, the quasi-steady-state method allows the measurement of very low lifetimes without fast electronics or short light pulses. The range of measurable lifetimes is only limited by signal strength.

2.4   Dangling bond recombination model

Recombination via dangling bonds (DB) can be described in analogy to SRH recombination. Modeling of the recombination processes is interesting for passivation purposes since important interface parameters can be inferred from the model. A dangling bond recombination model was established by Olibet *et al* [34]. The model was first proposed for recombination in bulk a-Si:H and then extended to the a-Si:H$/c$-Si interface.

2.4.1   Review of the recombination model by Olibet

Dangling bonds are electronic states within the band gap of a semiconductor, which can either act as trapping or as recombination centres. Demarcation levels are introduced in order to discriminate between trapping and recombination: E_{tn} is the demarcation level for electrons and E_{tp} is the demarcation level for holes. The position of these demarcation levels is defined by the equal probability of thermal emission and free carrier capture of an electronic state. For electronic states within the demarcation levels, the capture probability is higher than the re-emission probability. Electronic states in the energy interval between the demarcation levels therefore act as recombination centres and not as traps. Dangling bond states are mostly trivalent bonded Si atoms (Si_3). They can be occupied by zero, one or two electrons leading to three different charge conditions of the dangling bond states. When not occupied by an

electron, the dangling bond is positively charged and denoted as D^+. The neutral dangling bond is occupied by one electron and denoted as D^0. And the dangling bond is negatively charged (D^-) when occupied by two electrons. A representation of the density of states $N(E)$ in dependence of the energy E is shown in Figure 2.3(a). The correlation energy U is the difference between the transition levels D^+/D^0 and D^0/D^-. The energy U is required to place a second electron in the same Si_3 orbital. When most dangling bonds are in the neutral state, there are two possible paths events which lead to carrier recombination. The pathways are shown in Figure 2.3(b). Each path consists of two successive capture events. Pathway 1) describes the capture of a hole by D^0, followed by an electron capture. Pathway 2) describes the capture of an electron by D^0, followed by a hole capture. Along both paths, the recombination is limited by the less probable capture event (the smaller capture rate).

(a) Energy of recombination centres   (b) Electron-hole recombination through D^0
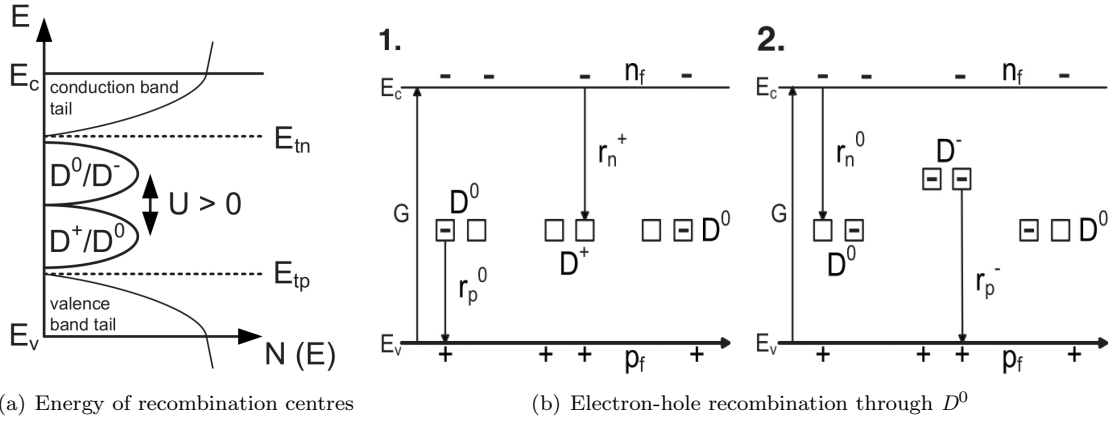
Figure 2.3: Dangling bond recombination model [34] a) Continuous distribution of recombination centres b) When most dangling bonds are in the neutral state there are two electron-hole recombination pathways: 1. hole capture followed by electron capture, and 2. electron capture followed by hole capture. Here D^+, D^0 and D^- are the positively, neutral and negatively charged condition of the dangling bonds, E_{tn} and E_{tp} are the demarcation levels, n_f and p_f are the free carrier densities, and r_p^0, r_n^+, r_n^0 and r_p^- are the capture rates.

2.4.2 Calculation of interface parameters

The interface recombination model can be applied to extract important information about surface passivation. The interface defect density N_s and the interface charge density Q_s can be extracted when the measured ECD minority carrier lifetime is fitted by the interface recombination model. In the dangling bond recombination model the interface recombination rate U_s is given by

$$U_s = \frac{n_s\sigma_n^0 + p_s\sigma_p^0}{\frac{p_s}{n_s}\frac{\sigma_p^0}{\sigma_n^+} + 1 + \frac{n_s}{p_s}\frac{\sigma_n^0}{\sigma_p^-}} v_{th} N_s \tag{2.19}$$

where σ_x are the different capture cross sections, n_f and p_f are the densities of free electrons and holes, v_{th} is the thermal velocity, and N_s is the interface defect density. The surface potential and the relation between interface recombination rate U_s and the effective surface recombination velocity S_{eff} can then be used to numerically determine N_s and Q_s as explained in by Bahardoust *et al* [35]. The interface defect density and the interface charge density are interesting parameters when comparing different passivation schemes because they are directly related to the two main passivation principles: a high defect density increases recombination by increasing the number of recombination centres, while a high fixed charge density reduces recombination by the field effect.

2.5   Film thickness measurement

Thickness measurement of thin films is a critical procedure for this project. Thickness measurement is not always straight forward, especially for ultra-thin layers. In this project, the SiO$_2$ thickness and the SiN$_x$ thickness are measured for all samples. The thickness of the ultra-thin silicon oxide layer is considered to have a strong influence on the surface passivation quality. Therefore, the oxide thickness must be carefully analyzed. The thickness of the silicon nitride layer should be kept constant for all experiments. The variation in SiN$_x$ thickness is analyzed as a source of error.

2.5.1   Spectroscopic ellipsometry (SE)

Spectroscopic ellipsometry (SE) is a powerful optical characterization technique for film thickness and optical constants of thin films. The advantages of SE include very high thickness sensitivity and very fast measurement which, in some applications, enables in-situ observation of material growth. The name ellipsometry comes from the fact that polarized light often becomes elliptically polarized upon reflection. A detailed description on theory and measurement methods of spectroscopic ellipsometry can be found in *Spectroscopic Ellipsometry: Principles and Applications* by Hiroyuki Fujiwara [36]. A quick overview of the basic principles is given here.

Experimenatl details of SE

In ellipsometry, the ratio of light polarized perpendicular to the plane of incidence (s-polarization) and light polarized parallel to the plane of incidence (p-polarization) is measured. The reflection coefficients for p- and s-polarizations differ significantly due to the difference in electric dipole radiation. Therefore p- and s-polarizations show different changes in amplitude and phase. In SE experiments, the two values Ψ and Δ are measured where Ψ is the amplitude ratio and Δ is the phase difference between the p-

and s-polarized light waves. The parameter ρ is the ratio between the complex reflection coefficient for light polarized parallel to the plane of incidence r_p and the light polarized perpendicular to the plane of incidence r_s. It is given by

$$\rho = \frac{r_p}{r_s} = tan\Psi e^{i\Delta} \tag{2.20}$$

where Ψ and Δ represent the change in amplitude and phase shift upon reflection. The rotating polarizer ellipsometer is a widely used ellipsometer system. In this technique, the parameters α and β are measured, which are independent of the intensity of the lamp. They are related to $tan\Psi$ and $cos\Delta$ via

$$tan\Psi = \sqrt{\frac{1+\alpha}{1-\alpha}} \cdot tanA \tag{2.21}$$

$$cos\Delta = \frac{\beta}{\sqrt{(1-\alpha^2)}} \tag{2.22}$$

where A is the analyzer azimuth. The measured data is not useful by itself. Modeling is necessary in order to relate Ψ and Δ to material properties and obtain the desired information (e.g. the film thickness). Some dielectric function models which are used for SE data analysis During SE data analysis are described in the following section. All models have free parameters and initial guesses for the optical properties of the materials are needed. In thin films the optical properties are usually quite different from bulk material. It can be quite difficult to find reasonable models and initial guesses for the optical parameters of thin-films.

Dielectric function models

The complex refractive index N is given by $N = n + i\kappa$, where n indicates the phase speed and κ describes the absorption. The dielectric function ϵ is given by $\epsilon(\lambda) = \epsilon_1(\lambda) + i\epsilon_2(\lambda)$, where ϵ_1 describes the polarization and ϵ_2 describes the absorption. The dielectric function depends on the wavelength λ of the incident light. The refractive index is related to the dielectric function via $\epsilon = n^2$. Optical spectra are measured in SE measurements. Analyzing optical spectra by simulation requires the optical constants as input. Fixed data sets, known as n-k files, can be used for well-known materials. Dielectric function models are used for more complicated samples under varying conditions. In dielectric function models, the model parameters are adjusted to achieve the best fit the measured spectrum. There are several models to characterize either the index of refraction n or for the dielectric function ϵ in dependence of energy (or wavelength).

Cauchy model

Cauchy's equation is the simplest model. The refractive index in dependence of the wavelength $n(\lambda)$ is given by

$$n(\lambda) = B + \frac{C}{\lambda^2} + \frac{D}{\lambda^4} + ... \tag{2.23}$$

where B, C and D are coefficients that can be determined for a material by fitting the equation to measured data at a known wavelength.

Sellmeier model

The Sellmeier model is an improved model based on the Cauchy model. The refractive index is given by

$$n(\lambda) = 1 + \frac{B_1\lambda^2}{\lambda^2 - C_1} + \frac{B_2\lambda^2}{\lambda^2 - C_2} + ... \tag{2.24}$$

where $B_{1,2}$ and $C_{1,2}$ are Sellmeier coefficients. The Sellmeier model can be employed to successfully model ultra-thin SiO_2 films [37]. However, the Cauchy model and the Sellmeier model are usually not in good agreement with experimental results for amorphous materials, and more sophisticated models are needed for the silicon nitride measurement.

Forouhi and Bloomer model

The Forouhi and Bloomer model [38] describes the extinction coefficient in dependence of the energy $\kappa(E)$ by

$$\kappa(E) = \frac{A(E - E_g)^2}{E^2 - EB + C} \tag{2.25}$$

where A, B, C and E_g are the fitting parameters. There are several problem associated with the Forouhi and Bloomer model which are described by Jellison et al [39].

Tauc-Lorentz model

The Tauc-Lorentz model [39] is a more realistic model. It is based on the Tauc joint density of states and the Lorentz model for the dielectric response for a collection of single atoms. The imaginary part of the dielectric function is given by

$$\epsilon_2 = \begin{cases} \dfrac{AE_0C(E - E_g)^2}{(E^2 - E_0^2)^2 + C^2E^2} \dfrac{1}{E} & \text{for } E > E_g \\ 0 & \text{for } E \leq E_g \end{cases} \tag{2.26}$$

where E_0 is the peak in the joint density of states, E_g is the optical band gap, C is the broadening parameter, and A is a prefactor which includes the optical transition matrix elements. The Tauc-Lorentz is an empirical expression which is only valid for interband transitions. The real part of the dielectric function is given by the Kramers-Kronig integral

$$\epsilon_1(E) = \epsilon_1(\infty) + \frac{2}{\pi} P \int_{E_g}^{\infty} \frac{\xi \epsilon_2(\xi)}{\xi^2 - E^2} d\xi \qquad (2.27)$$

where P is the Cauchy principal part of the integral. In general it is assumed that $\epsilon_1(\infty) = 1$. It can be greater than 1 if there is a significant optical transition at an energy greater than the sampled energy by the ellipsometer. In the Tauc-Lorentz model there are therefore 4 fitting parameters. The Tauc-Lorentz model is considered the best model for amorphous films and will be used for the SiN_x thickness measurement. The initial guesses for the parameters were chosen according to [30].

2.5.2 X-ray photoelectron spectroscopy (XPS)

Photoelectron spectroscopy (XPS) is a photoemission technique in which allows to measure the elemental composition and the electronic state of the elements near the surface in a material. A nice introduction into XPS techniques can be found in *Surface Analysis by XPS and AES* by J. F. Watts and J. Wolstenholme [40] and a short overview will be given here.

Experimental details of XPS

XPS is based on the photoelectric effect: the sample is irradiated with X-ray photons of energy $h\nu$ and electrons from the core of the atoms are ejected. The energy of the emitted photoelectrons is then analyzed by an electron spectrometer and the data is presented as a graph. The number of counts (intensity) are shown over the electron energy. A spectrometer measures the kinetic energy of the electron E_{kin} which depends on the binding energy of the electron E_{bind} in the sample, the photon energy, and the work function of the spectrometer

$$E_{bind} = h\nu - E_{kin} - \Phi \qquad (2.28)$$

where the photon energy $h\nu$ and the work function of the spectrometer Φ are known from the experimental setup. The quantity of interest is the binding energy of the electron which depends on the atom and its chemical environment. Each element has its characteristic distribution which corresponds to the electronic states of the electrons. From the measured signal it is therefore possible to study the elements

in a material and their electronic states. XPS is a measurement technique to analyze the surface of a sample. The depth from which information can be derived is a few nanometres and depends on the attenuation length of the electrons which is related to their inelastic mean free path. The finite mean free path of the electrons within a solid can be exploited to measure properties of a thin film using a technique called angle resolved XPS.

Angle resolved x-ray photoelectron spectroscopy (ARXPS)

Angle resolved x-ray photoelectron spectroscopy (ARXPS) is a powerful and non-destructive depth profiling method. In conventional XPS measurements, the analysis direction is at a direction normal to the surface of the sample. Due to the finite mean free path the analysis depth is usually limited by approximately 3λ, where λ is the attenuation length of the electrons. In ARXPS, electrons are detected at an angle Θ with respect to the surface normal. The information depth d is given by $3\lambda \cos \Theta$. The relative sampling depths at different take-off angles are illustrated in Figure 2.4.
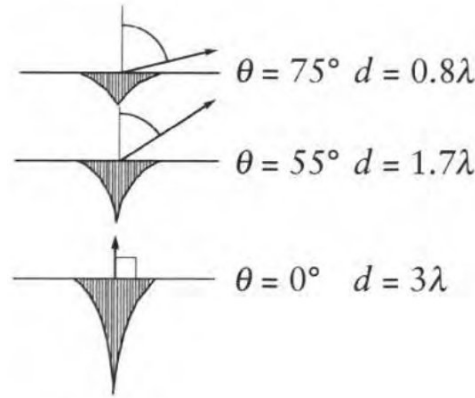
Figure 2.4: Schematic illustration of sampling depth d as a function of take-off angle Θ in ARXPS measurements [40]. The maximum sampling depth is approximately 3λ due to the finite mean free path of electrons.

Modern instruments are capable of parallel collection of angle resolved data without rotating the sample. Parallel ARXPS ensures that all data is measured at the same point and it allows for the measurement of large samples which could not be tilted in a conventional XPS spectrometer.

Thin film thickness measurement using ARXPS

The intensity of electrons I from all depths greater than d is given by the Beer-Lambert law

$$I = I_0 e^{-d/\lambda \cos \Theta} \tag{2.29}$$

where λ is the attenuation length, Θ is the take-off angle with respect to the surface normal, and I_0 is the intensity from an infinitely thick substrate. Using ARXPS, the thickness d_A of a thin film of material A on a substrate B can be extracted. To obtain the signal I_A from material A we have to take the signal for an infinitely thick layer of the material I_A^∞ and subtract the signal that we would expect for depths greater than d_A

$$I_A = I_A^\infty \left(1 - e^{-d_A/\lambda_A \cos \Theta} \right) \tag{2.30}$$

where λ_A is the attenuation length for electrons from material A. For the signal I_B from material B we assume that the substrate is infinitely thick and the signal arriving at the B-A interface is therefore given by I_B^∞. The signal is then attenuated by passing through layer A and the signal emerging at the surface is given by

$$I_B = I_B^\infty e^{-d_A/\lambda_{B,A} \cos \Theta} \tag{2.31}$$

where $\lambda_{B,A}$ is the attenuation length in the layer A for electrons emitted from layer B. At the surface we can measure the ratio of both signals I_A/I_B

$$\frac{I_A}{I_B} = \frac{I_A^\infty}{I_B^\infty} \frac{\left(1 - e^{-d_A/\lambda_A \cos \Theta} \right)}{e^{-d_A/\lambda_{B,A} \cos \Theta}} \tag{2.32}$$

and we can extract the thickness d_A by fitting the measured signal.

Suboxides at the interface

The binding energy of the electrons strongly depends on their chemical environment. We use ARXPS to measure thin SiO_2 films. The signals for sub-oxides are shifted in energy with respect to the bulk silicon oxide peak. By fitting the measured data with separate curves for each sub-oxide species we can extract information on the existence of sub-oxides. For our purpose we are interested in analyzing the sub-oxides of silicon at the Si/SiO_2 interface.

Chapter 3

Materials and Methods

In this chapter, the materials and methods of our research are presented. In the first part, the materials are described and a detailed explanation of the design and the setup of the ozone oxidation chamber is given. In the second part, the parameters of different measurement devices (spectroscopic ellipsometry, x-ray photoelectron spectroscopy, lifetime measurement tools) are described and example measurements are shown. Finally the experimental methods for the oxide growth and the lifetime study are presented.

3.1   Materials

3.1.1   Wafers, chemicals and further materials

The following silicon wafers were used for our experiments:

Type	Size	Orientation	Quality	Thickness	Surface	Resistivity
p	4 inch	$< 100 >$	CZ	500 ± 25 μm	DSP	10-20 Ωcm
n	4 inch	$< 100 >$	CZ	500 ± 25 μm	DSP	10-20 Ωcm
n	4 inch	$< 100 >$	FZ	280 ± 10 μm	DSP	1-5 Ωcm

Table 3.1: Wafer properties. DSP stands for double-side polished.

Czochralski (CZ) prime wafers were used for the extensive passivation study. The wafers were purchased from University Wafers (p-type wafers) and Silicon Quest International (n-type wafers). High quality n-type float zone (FZ) wafers from Topsil were used for FT-IR experiments. Resistivity of wafers was determined using Four Dimensions Six-Point-Probe Meter Model 101C in Pratt cleanroom. The native oxide layer of silicon wafers was removed by etching in 2 % hydrofluoric acid (HF) for 5 min. Hydrofluoric acid (49 %, CMOS grade) was used from J.T. Baker.

3.1.2   Ozone oxidation chamber

The ozone oxidation chamber was planned designed and set up during this project.

Planning of the oxidation chamber

We started from the scratch by identifying the requirements of the experimental setup:

- Closed oxidation chamber with ozone in oxygen atmosphere

- Controllable sample heating (up to 450 °C)

- Homogeneous oxidation of samples (maximum size: 6 inch wafer)

- Installation of samples at a variable height above the heater surface

- Possibility to introduce other gases

- Safe workplace conditions (see also 3.1.2)

Experimental setup

The requirements of the experimental setup were translated into the experimental schematic shown in Figure 3.1(a). The main components of the experimental setup are: an ozone generator, the custom designed oxidation chamber with a heating plate and a temperature control unit, and an ozone destructor. The inner dimensions of the oxidation chamber are 41 x 41 x 15 cm^3. It consists of a bottom plate and a lid which is attached to the bottom plate using two hinges. The chamber is sealed using a Viton o-ring. Three gas inlets are connected to the oxidation chamber, the first inlet being connected to the ozone generator, the second inlet being connected to an argon bottle (for purging of the chamber), and the third inlet being available for the introduction of additional gases. The gas is introduced into the chamber using cylindrical pipes with holes (purple) in order to reach a more homogeneous gas flow at the sample location. Gas tubes, connections and valves are Swagelok parts. A 18 x 18 x 1.5 cm^3 stainless steel plate is used as a heating plate. The plate is heated using resistive heating of 5 cartridge heaters with 200 W each. Two K-type thermocouples, which are attached to the heater, are used for temperature feedback to the temperature control unit. The samples can be installed at different heights above the heater plate. Four alligator clips allow the installation at a height of 10 mm above the surface, ceramic pearls of different size can be used to place samples closer to the heater surface, or the samples can be placed on the heater directly. Feedthroughs with CF flanges are used for thermocouple connections and electrical connections. At the gas outlet, a catalytic ozone destructor is used to decompose the ozone

before the gas is transported to the window and released in the air. For a detailed list of chamber parts please refer to Appendix A.1.
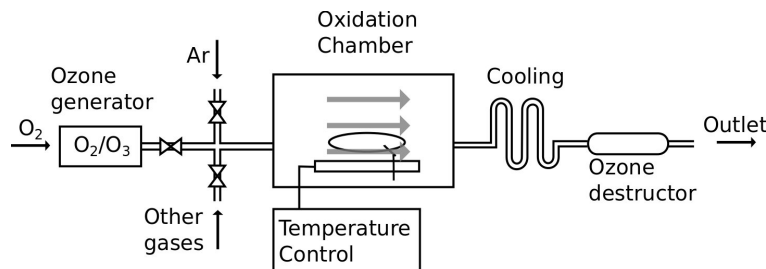
(a) Schematic of experimental setup
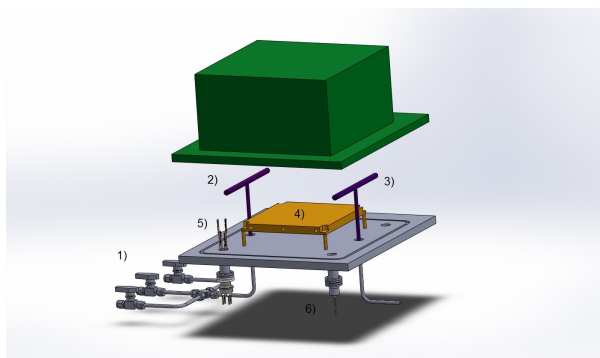
(b) Drawing of ozone oxidation chamber

Figure 3.1: Chamber schematic and drawings. a) The ozone oxidation chamber consists of an ozone generator, the oxidation chamber with a heating plate, a temperature control unit, and an ozone destructor. b) Solidworks drawing of the custom designed chamber parts: 1) gas valves, 2) gas inlet, 3) gas outlet, 4) heater plate, 5) thermocouple connections, 6) power supply connections.

Installation of the chamber

The ozone oxidation experiment was set up in the lab GB250B as shown in Figures 3.2.

(a) Experimental table   (b) Chamber parts   (c) Experimental setup   (d) Experimental setup
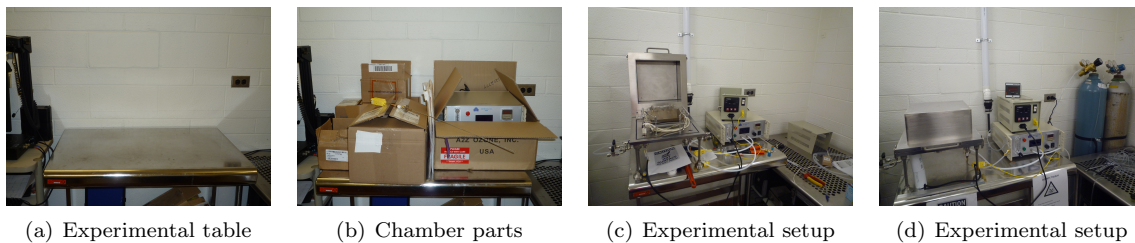
Figure 3.2: Experimental setup. The ozone oxidation chamber consists of standard parts (commercially available) and custom designed parts (fabricated by the machine shop at the UofT). The chamber was installed on an experimental table in the lab GB250B.

The main oxidation chamber, the ozone generator, and the temperature control unit are placed on the experimental table. The gas bottles (oxygen and argon) are secured to the wall next to the experimental

table. The exhaust gas is transported to the ozone destructor and then transported to the window and released into the air.

Safety considerations

According to the Canadian Workplace Hazardous Materials Information System (WHMIS) ozone has the following classifications:

Figure 3.3: WHMIS classification of ozone.

A - Compressed gas

C - Oxidizing material

D1A - Poisonous and infectious material - Immediate and serious effects - Very toxic

D2A - Poisonous and infectious material - Other effects - Very toxic

D2B - Poisonous and infectious material - Other effects - Toxic

F - Dangerously reactive material

The ground-level ozone concentration in southern Ontario is around 40 parts per billion [41]. The American National Standards Institute / American Society for Testing and Materials (ANSI/ASTM) exposure limit is 0.1 ppm time-weighted average for 8 h (0.3 ppm for short term exposure). In order to minimize the risk of ozone exposure, the experimental chamber was completely sealed, and a fan with a power of 600 m^3/h was installed in the lab to ensure a gas exchange. The ozone concentration in the lab was measured be the Environmental Health and Safety Department. The ozone concentration in the lab was measured for 15 minutes while running an experiment under normal experimental conditions (sealed chamber, 2 L/min gas flow, maximum ozone generation rate). The following values were obtained:

- Minimum concentration: 0.008 ppm

- Maximum concentration: 0.018 ppm

- Average over 15 minutes: 0.016 ppm

The ozone concentration was found to be more than 5 times smaller than the work place exposure limit and even smaller than the average concentration in southern Ontario. An additional test was performed in order to characterize the ventilation system of the lab. The oxidation chamber was run for 15 minutes at normal experimental conditions. The chamber was then opened for 15 seconds without stopping the gas flow. The ozone concentration immediately jumped to 0.45 ppm and decayed to < 1 ppm after 12 minutes. This experiment underlines the importance of the purging step after oxidation. We would like to emphasize that we strictly avoid this scenario during normal operation by purging the experiment with argon for 30 minutes before opening the chamber. In case of failure to do so the room must be left immediately. The ventilation system successfully decreases the ozone concentration. The lab can be safely entered after 15 minutes if the chamber was opened for < 15 seconds during ozone exposure. We also considered the effect of an increased oxygen concentration. The gas mixture for our experiments contains < 1 % ozone in oxygen. If the ambient ozone concentration is below 0.1 ppm then the additional oxygen is below 10 ppm. By monitoring the ambient ozone concentration it can automatically be concluded that the ambient oxygen concentration does not significantly change the normal atmospheric values (approximately 21 %).

Ozone concentration

An A2Z Model 2GLAB ozone generator was used for ozone generation. The generator has an ozone output of $c_{gen} = 1$ g/hour. We usually chose a flow rate of $Q = 2$ L/min $= 120$ L/hour for our experiments. The ozone flow is therefore given by $1/120$ g/L which corresponds to $22.4/120$ g/mol, using that the molar volume V_{mol} of an ideal gas is $V_{mol} = 22.4$ L/mol. Since the ozone concentration is very small, we can assume the molar mass of the total gas flow to be equal to the molar gas of oxyen $M_{O_2} = 32$ g/mol. The ozone concentration entering our experimental chamber is therefore given by $c_{gas} = 22.4/(M_{O_2} \cdot Q) = 0.58$ %. The chamber volume is $V_{ch} = 13$ L. At a flow rate of 2 L/min the gas inside the chamber is exchanged approximately every 7.5 minutes. The ozone concentration can be changed by changing the flow rate Q. However a smaller flow rate is related to a longer gas exchange time. Under atmospheric conditions ozone decays to oxygen $2O_3 \rightarrow 3O_2$, and the half life of ozone is $t_{1/2} \approx 30$ min. We assume that the number of ozone particles n can be described by an exponential law $n = n_0 e^{-t/\tau}$, where n_0 is the starting concentration, and the decay constant τ is given by $t_{1/2}/\ln(2)$. After 7.5 minutes the number of ozone particles is reduced to $0.84 \cdot n_0$. The chamber is designed in order to have a gas flow which is almost laminar at the position of the samples. Considering that the gas inlet is close to the sample position, and assuming a laminar flow, the ozone decay at the sample position can be neglected, and the ozone concentration can be assumed to be constant.

3.1.3   Fabrication and measurement equipment

The following section gives a brief introduction to the fabrication and measurement tools which were used in this project. The fabrication and measurement parameters are presented.

Plasma-enhanced chemical vapour deposition

Oxford PlasmaLab 100 direct rf PECVD system in Bahen cleanroom was used for the SiN_x depositions for native-SiO_2/SiN_x passivation studies. The optimal deposition conditions for passivation purposes were found by Chowdhury *et al* [26]. The following precursor gases were used: NH_3 at a flow rate of 50 sccm and 5 % silane in nitrogen ($SiH_4 + N_2$) at a flow rate of 350 sccm. Depositions were carried out for 4.25 min at 400 °C, a chamber pressure of 1 Torr, and a plasma power of 25 Watt.

Unfortunately the Oxford PECVD system in Bahen cleanroom was shut down for a long period of time for maintenance and repair during our final passivation study. Alternatively, the SiN_x depositions were carried out by Dr. Todd W. Simpson at the University of Western Ontario using a capacitively coupled plasma PECVD system. The recipe was slightly adjusted to meet the requirements of the system while keeping the gas precursor gas ratio and the deposition temperature the same. The following precursor gases were used: NH_3 at a flow rate of 75 sccm and 5 % silane in nitrogen ($SiH_4 + N_2$) at a flow rate of 525 sccm. Deposition were carried out at 400 °C, a chamber pressure of 1 Torr, and a plasma power of 12 Watt. Two test samples (1/4 wafer, n-type, FZ, 1-5 Ωcm) were prepared and coated with SiN_x at the University of Western Ontario in order to compare the SiN_x quality to our previous results. We used one sample with 1 nm native oxide and one sample with 1 nm UV-ozone grown oxide (using the UVOCS Model T0606B UV/ozone cleaning system for 1 h). The obtained lifetimes are 1027 μs and 1001 μs for the native oxide and the UV-ozone oxide respectively. Those lifetimes are similar to the results by Chowdhury *et al*. We conclude that the PECVD system at the University of Western Ontario is capable of producing SiN_x with similar passivation characteristics.

Lifetime measurements

The excess carrier density (ECD) dependent effective minority carrier lifetime τ_{eff} was measured using a Sinton WCT-120 silicon wafer lifetime tester shown in Figure 3.4(a). Sinton WCT-120 allows both transient and quasi-steady-state photoconductance (QSSPC) lifetimes measurements. Spatial distributions of the lifetime were obtained using a Semilab WT-2000 microwave photoconductance decay (μPCD) system shown in Figure 3.4(b) with Wintau32 software.

(a) Sinton

(b) Semilab

(c) SE

(d) PARXPS

Figure 3.4: Measurement devices: a) Sinton lifetime tool b) Semilab lifetime tool c) Sopra sepctroscopic ellipsometer d) Thermo Scientific parallel angle-resolved x-ray photoelectron spectroscopy. Pictures are downloaded from the company webpages.

Sepctroscopic ellipsometry

The Sopra GES-5E spectroscopic ellipsometer shown in Figure 3.4(c) with WinSE software was used for thickness measurements of silicon oxide and silicon nitride. The incident angle was set to 75° which corresponds to the Brewster angle of silicon. The values were scanned at an energy of 1-5 eV with a resolution of 0.02 eV.

Parallel angle-resolved x-ray photoelectron spectroscopy

The Theta Probe parallel angle-resolved x-ray photoelectron spectroscopy system from Thermo Scientific shown in Figure 3.4(d) was used with Thermo Avantage software for thickness measurements of ultra-thin silicon oxide films. The obtained Si_{2p} data was fitted using mixed Lorentzian and Gaussian functions with

a modified Shirley background. The ratio of elemental silicon to silicon oxide was calculated for different angles. The experimental data was compared to theoretical calculations for oxide layers with different oxide thicknesses using the Beer-Lambert equation. The thickness of the oxide layer was obtained from the best fit of experimental and theoretical data.

Fourier-transform infrared absorption spectroscopy

Fourier-transform infrared (FT-IR) absorption spectra were measured using Perkin Elmer System 2000. Samples were measured in transmission mode at perpendicular incidence. The FT-IR signal from a sample with a silicon oxide layer was measured and subtracted from the signal of an oxide-free silicon sample. The signal after subtraction of the reference signal is directly related to the thin silicon oxide film. FT-IR data was taken from 20 cycles between 450 cm^{-1} and 5200 cm^{-1} at a resolution of 16 cm^{-1}. The wide wavelength range allowed us to distinguish between vibrational peaks and background noise for example due to the Fabry-Perot interference of the thin film. Our analysis was based on the Si-O anti-symmetric stretching vibration with absorption frequencies of ~1065 cm^{-1} (TO frequency) and ~1250 cm^{-1} (LO frequency). In our experiments we can only observe the TO frequency. It has been previously reported by other groups that the LO frequency cannot be detected in transmission geometry with perpendicular incidence [42]. High quality float zone wafers were used for the FT-IR study after we ha found that Czochralski wafers can not be used due to their high oxygen content. The large signal due to the oxygen impurities around ~1065 cm^{-1} overlaps with the desired thin-film SiO_2 signal. The large amount of oxygen impurities is well known in literature [43]. In our experiments we found that the oxygen distribution throughout the wafer is inhomogeneous, since it does not cancel out when subtracting the signal from an identical reference sample. The inhomogeneity of the oxygen content was new to us. It makes CZ wafers unsuitable for the study of silicon oxide vibration frequencies.

3.2   Data analysis

The data analysis of lifetimes measurements and film thickness measurements is explained in the following section. Illustrative example measurements are shown.

3.2.1   Lifetime measurements and recombination fitting

The minority carrier lifetime can be directly obtained from the photoconductance decay measurement. The Semilab measurement gives a spatial distribution of the lifetime as shown in Figure 3.5(a). More detailed data analysis is possible using the Sinton lifetime tester. The excess carrier density (ECD)

(a) Semilab data   (b) Sinton data and fitting
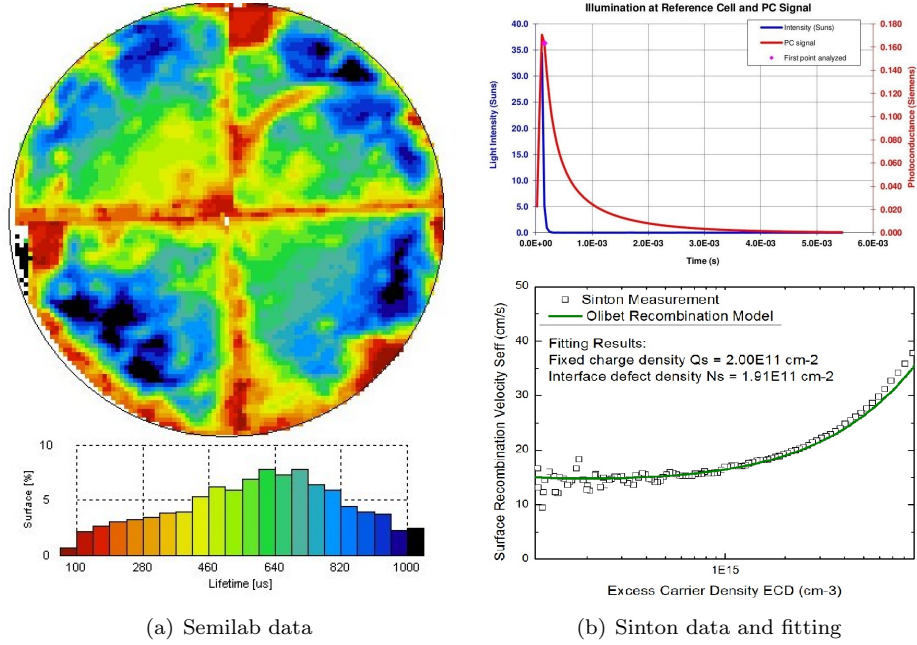
Figure 3.5: Example measurement and fitting of lifetime data. a) Lifetime data with spatial resolution can be obtained using Semilab measurement. The data of four 1/4 wafer is samples is shown. b) Excess carrier dependent minority carrier lifetime data can be obtained using Sinton measurement (top graph). The Sinton data can be fitted using the interface recombination model (bottom graph) to extract the defect density and the fixed charge density.

dependent minority carrier lifetime measurement was measured as shown in the top graph of Figure 3.5(b). According to official conventions, the lifetime at an excess carrier density of 1E15 cm^{-3} was reported and used for SRV calculations. The excess carrier dependent lifetime was fitted using the dangling bond recombination model described in Section 2.4. The fitted data is shown in the bottom graph of Figure 3.5(b). It allowed us to extract two parameters which are relevant for surface passivation: the defect density N_s and the fixed charge density Q_s. A fitting program was used, which was developed by Bahardoust *et al* [35]. The fitting needs the capture cross sections σ for holes and electrons as parameters. The exact values of the capturing cross sections are not known and are under discussion in literature. We considered two different sets of values for our data analysis. Leendertz *et al* have proposed the values $\sigma_n^0 = \sigma_p^0 = 10^{-17}$cm^2 and $\sigma_n^+ = \sigma_p^- = 10\sigma_n^0$ [44]. Bahardoust *et al* have used the values $\sigma_p^0 = 10^{-16}$cm^2 and the ratios $r_1 = \sigma_p^-/\sigma_p^0 = \sigma_n^+/\sigma_n^0 = 50$ and $r_2 = \sigma_n^0/\sigma_p^0 = 0.25$ [35]. We achieved the best fit by using $r_1 = 1$, and the parameters proposed by Bahardoust *et al* otherwise. We admit that there may be a large error associated with this assumption. The literature values differ a lot, and they have been originally proposed for *a*-Si:H passivation instead of SiN$_x$ passivation. The obtained numbers for the defect density N_s and the fixed charge density Q_s can therefore not be seen as absolute values. However the trend in those values for different passivation layers can be considered as additional

information in order to understand the underlying microscopic effect of the surface passivation.

3.2.2   Spectroscopic ellipsometry

The measured SE data was fitted using the Winelli II software in order to obtain the film thickness and the refractive index of the SiO_2 and SiN_x layers. For thin silicon oxide films, the Sellmeier standard dielectric function was used because it showed the best agreement with literature values of the native oxide growth. Other publications [45] confirmed that the Sellmeier model is suitable for silicon dioxide. The start values ($A = 1.45$ and $B = 9E\text{-}3$) were chosen according to the Sopra Measurement (1997) which is provided by the Winelli software as SiO2-S2 file. For amorphous silicon nitride films, the Tauc-Lorentz dispersion model (with one transition) was used, as suggested by many different publications. The starting values were chosen as $\epsilon_1(\infty) = 1$ (fixed), $E_g = 3$ eV, $A = 80$ eV, $E_0 = 10$ eV and $C = 6$ eV. Figure 3.6 shows an example of measured and the fitted values for $\tan\Psi$ and $\cos\Delta$ for a 3 nm SiO_2 film on silicon). The fitting was done using the Sellmeier dielectric function model as described.

(a) Measurement and fitting of cos∆   (b) Measurement and fitting of tanΨ
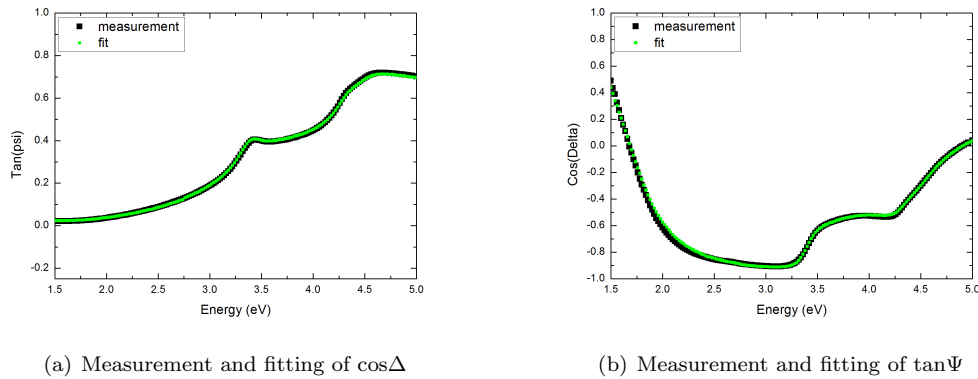
Figure 3.6: Example: measurement and fitting of SE parameters. The data was taken from a measurement of 3 nm SiO_2 on a crystalline silicon substrate.

3.2.3   Angle-resolved XPS

Using angle-resolved XPS, the O_{1s}, C_{1s} and Si_{2p} peaks were measured for 15 different incidence angles between $25.36°$ and $78.13°$. A comparison of the abundance of different elements allows us to roughly map the atomic distribution over the incidence angle as shown in Figure 3.7(a). From this plot we can detect carbon impurities and adsorbates near the surface. For more sophisticated overlayer thickness analysis, we restrict the analysis to the Si_{2p} peaks. Figure 3.7(b) shows the measured Si_{2p} data at an incidence angle of $51°$. The oxide-Si_{2p} electrons have slightly higher binding energies than the elemental-

Si_{2p} electrons. Both Si_{2p} peaks were fitted using doublets, since the signal consists of the two different peaks $Si_{2p_{1/2}}$ and $Si_{2p_{3/2}}$ due to spin-orbit coupling. The oxide overlayer thickness can be calculated from the ratio of oxide Si_{2p} over elemental Si_{2p} in dependence of the incidence angle.

(a) Atomic distribution

(b) XPS Si_{2p} data
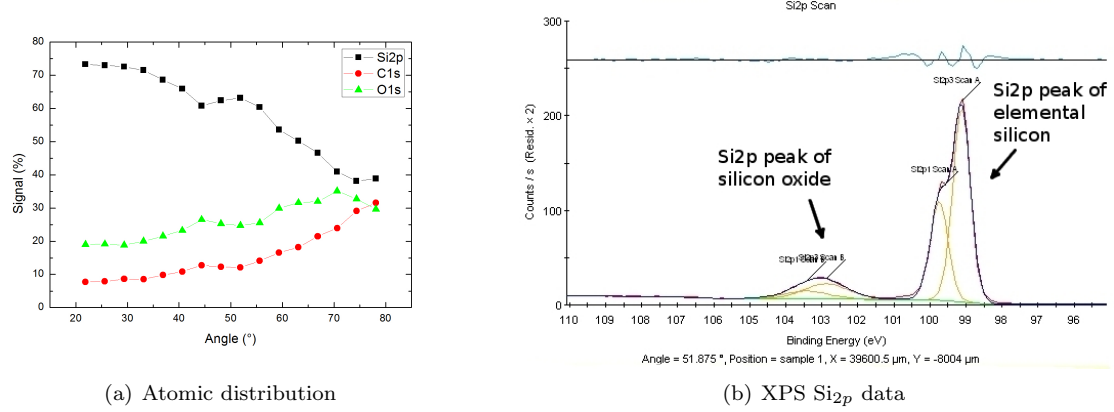
Figure 3.7: Example: XPS data and analysis. a) The atomic distribution can be calculated by comparing the elemental signals of O_{1s}, C_{1s} and Si_{2p}. The incidence angle can then be related to the depth in the sample. b) The thickness of a SiO_2 overlayer can be calculated by comparing the ratio between the elemental Si_{2p} signal and the oxide Si_{2p} which is slightly shifted to higher energies.

3.3 Experimental methods

Two main experimental studies were performed in this project besides a variety of smaller experiments. The oxide growth in our custom-built oxidation chamber was characterized, and the passivation quality of our novel bilayer passivation scheme was analyzed in dependence on varying oxidation parameters.

3.3.1 Ozone oxide growth study

The oxide growth on crystalline silicon strongly depends on the oxidation conditions, e.g. temperature and oxidation time. The oxidation saturates at different oxide thicknesses depending on the conditions. Refer to the Appendix Section D for a review on silicon oxidation by ozone. An extensive study was performed in order to anlyze the oxide growth in our custom built oxidation chamber. For the first rough calibration n-type and p-type CZ silicon wafers with a resistivity 15 Ωcm were used. The sample size was 1 x 1 cm^2. The samples were oxidized under different conditions and the oxide thickness was subsequently measured using SE on both sides of the sample and at two different sites across the sample. The rough calibration curves (which are not shown here) allowed us to specify the oxidation conditions for the passivation study. Detailed graphs were measured using 1/4 wafer samples (n-type, CZ, 15 Ωcm).

The oxide thickness was measured on 6 spots across the sample for better statistics on the homogeneity. The samples were subsequently used for the passivation study.

3.3.2 Surface passivation study

An extensive lifetime study was performed in order to find the optimal parameters for surface passivation. N-type CZ silicon wafers with a resistivity of 15 Ωcm were used unless otherwise noted. The size of the samples was one quadrant of a 4 inch diameter wafer. Two samples were oxidized simultaneously during every experiment. One sample was installed at a height of 10 mm above the heater surface (using alligator clips) and the second sample was placed directly on the heater surface. Some experiments were carried out with three samples where the third sample was placed directly on the heater surface and then flipped over and re-oxidized in an additional oxidation using the same parameters. Those samples are referred to as re-ox. The oxide thickness of the samples was characterized using SE after the oxidation. The samples were then coated with 80-100 nm of SiN_x at the University of Western Ontario. The samples were characterized using Semilab and Sinton lifetime measurement. The interface parameters Q_s and N_s were calculated using the interface recombination model.

Remark: The layer nitride thickness varied between 80-100 nm although the same recipe was used for all SiN_x coatings. The changes in nitride thickness can be explained by slight variations of the PECVD chamber temperature during deposition (the temperature of the PECVD system at the University of Western Onatrio cannot be held constant at 400 °C because it is designed for temperatures below 350 °C). Based on previous results by Chowdhury *et al*, we assume that the exact SiN_x thickness does not influence the passivation quality.

Chapter 4

Results and Discussion

In the following Chapter we present the results of this project. In the first part, we present the native oxide growth on a pure silicon wafer. In the second part, we show the calibration of our ozone oxidation chamber and then present the ozone oxide growth for different oxidation conditions. In the third part, we present the results of an extensive passivation study using ozone-SiO_2 and PECVD-SiN_x as passivation scheme. The term 'ozone oxide' always refers to a silicon oxide layer grown in our custom-built ozone chamber unless otherwise noted.

4.1 Native oxide growth

In this experiment, we measured the native oxide growth on crystalline silicon over 2 months. The main goal of this experiment was to find out if spectroscopic ellipsometry is suitable for thickness measurements of ultra-thin silicon oxide films. A double-side polished n-type FZ wafer with 77.5 Ωcm resistivity was used (the choice of the wafer was based on the availability of wafers). A 3 x 3 cm^2 sample was dipped in 2 % HF to etch the native oxide and then stored in a petri dish under atmospheric environment. The silicon oxide film thickness was measured using spectroscopic ellipsometry on four different points across the sample. The data of the different measurement points was averaged in order to have some statistics. The first measurement was done immediately after HF dipping, and the following measurements were done after representative time intervals. The SE data was analyzed using a variety of different dielectric function models (data not shown). Two values were evaluated in order to find the most realistic dielectric function model: 1) The goodness of fit was compared based on the coefficient of determination R^2, and 2) the calculated oxide thickness was compared to literature values of the native oxide growth. The best results were obtained using the Sellmeier dielectric function model as shown in Figure 4.1. We can

see that the first layers of native oxide grew back immediately after the HF dipping, and the first 4 Å are formed within the first 10 hours. Please note that an exact time resolution in the first hours is not possible due to the high energy resolution of the SE measurement (the measurement of four spots on the sample at a resolution of 0.01 eV takes 1.5 hours). The oxide thickness was measured using angle-resolved XPS for additional verification. The XPS thickness values are comparable to the SE thickness values (the deviation is <2 Å). From the accuracy of the measurement, and the perfect agreement with literature values (see inset of Figure 4.1), we conclude that spectroscopic ellipsometry is suitable for thickness measurements of ultra-thin silicon oxide films (with a thickness resolution of a few Å).
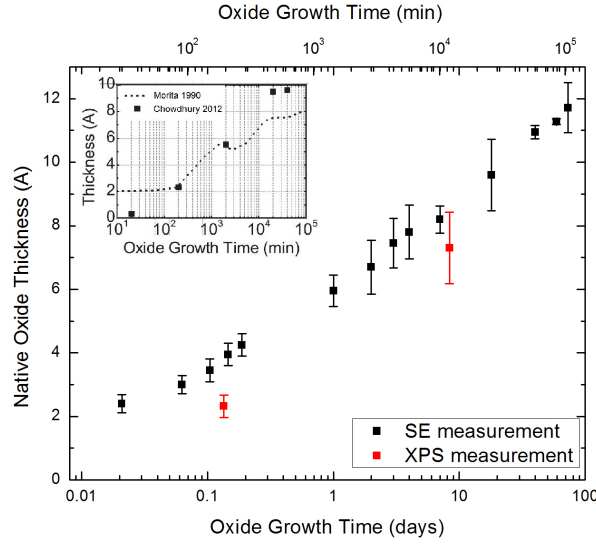
Figure 4.1: Native oxide growth measured by spectroscopic ellipsometry. Inset: literature values as reported by Chowdhury *et al* [26]. The native oxide growth measured by SE is in agreement with XPS measurements and with previously reported results.

4.2 Oxidation chamber temperature calibration

The oxidation chamber is heated using a heating plate with five cartridges. The design of the heating plate allows us to reach heater temperatures up to 450 °C. The temperature is controlled using a feedback temperature controller with a thermocouple attached to the heater plate. Samples can be installed at different heights above the heater surface. Temperature calibration is needed to relate the heater temperature to the actual temperature of the sample. In order to calibrate the sample temperature, a test wafer with two attached thermocouples was installed inside the chamber. The plug on the calibration feedthrough was removed and a plastic adapter was fixed on the feedthrough to guide the thermocouple wires. The chamber was closed and the calibration curves were taken at an argon flow of 2 L/min.

Please note that it is not possible to do the calibration using ozone because the plastic adapter does not seal the chamber sufficiently! Calibration curves were taken at a heater temperature of 450 °C and a sample height of 10 mm, 3 mm, 1.5 mm and 0.15 mm. From the detailed calibration curves, which are shown in Figure 4.2(a), we obtained equations which allow us to calculate the sample temperature at a given heater temperature and sample height. The results are shown in Figure 4.2(b).

(a) Calibration data

(b) Calibration equations
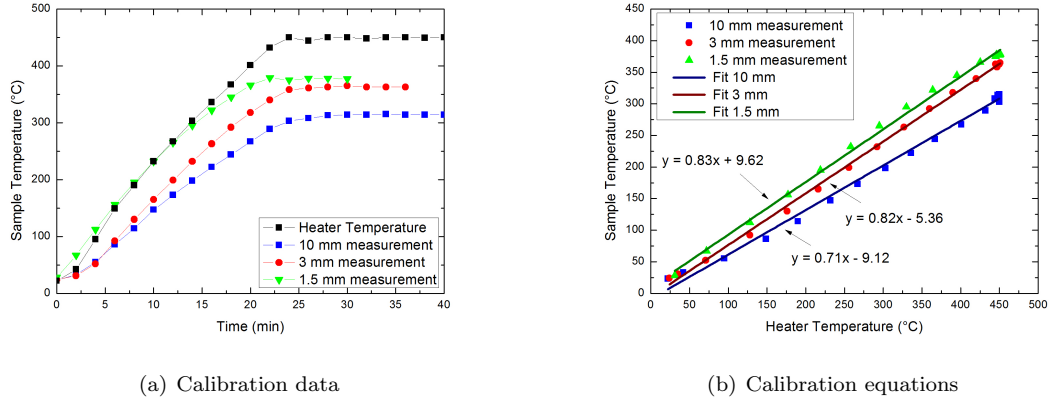
Figure 4.2: Temperature calibration. The sample temperature can be determined from the heater temperature and the sample height. The relation between the sample temperature and the heater temperature are shown in blue, red, and green for 10 mm, 3 mm, and 1.5 mm sample height respectively.

4.3   Ozone oxide growth

A variety of experiments was performed in order to study the oxide growth under different oxidation conditions. N-type CZ wafer with a resistivity of 15 Ωcm were used for the experiments. The size of the samples was one quadrant of a 4 inch diameter wafer. The oxide thickness was measured using spectroscopic ellipsometry on 6 spots across the sample and on both sides of the sample. The data of the different measurement points on each side of the sample was averaged in order to have some statistics. We compare the resulting oxide thickness for different parameters. Every data point in the results section represents a separate sample, unless otherwise noted. The error bar of a data point corresponds to the variation in the oxide thickness across the sample.

4.3.1   Time dependence

The time dependence of the oxide growth was studied, and the results are presented here. Samples were installed at different sample heights (10 mm or 0 mm above the heater surface), and then oxidized for different periods of time. The oxide thickness was measured using spectroscopic ellipsometry. Represen-

tative graphs are shown in Figure 4.3 for oxidation at 450 °C and 25 °C respectively. We found a fast

oxide growth at the beginning of the oxidation, and decreasing oxidation rates for longer exposure times.

In all experiments, the oxide growth saturated after a certain oxidation time. This result is in agreement

with findings in literature (compare to Fink *et al* [46]). The saturation time and the saturation oxide

thickness depend on the sample temperature. The oxide growth at 450 °C saturated after 8 hours while

the oxide growth at room temperature already saturated after 45 minutes.
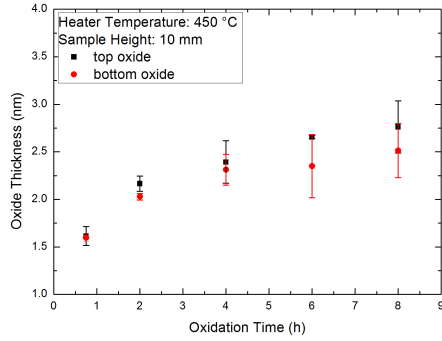
(a) Oxide growth at 450 °C and 10 mm sample height

(b) Oxide growth at 450 °C and 0 mm sample height
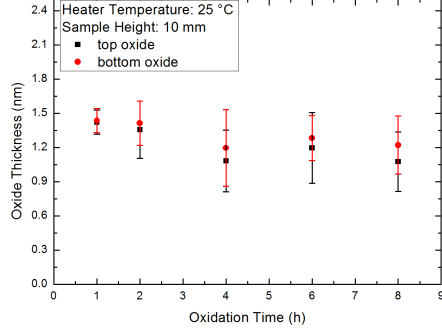
(c) Oxide growth at 25 °C 10 mm sample height
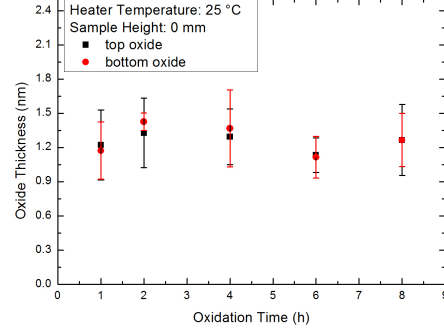
(d) Oxide growth at 25 °C and 0 mm sample height

Figure 4.3: Time dependence of oxide growth. The oxide growth for oxidation at a heater temperature of 450 °C is shown at a sample height of 10 mm in a) and 0 mm in b). The oxide growth for oxidation at room temperature is shown at a sample height of 10 mm in c) and 0 mm in d). A saturation of the oxide growth can be observed for all samples. The difference between the oxide thickness on the top and on the bottom of the sample increases when the sample is positioned closer to the heater surface due to the absence of ozone at the bottom of the sample.

We notice a higher oxide thickness on the top of the samples which were oxidized at elevated temper-

atures. This is a reproducible characteristic of our setup and can be related to the higher ozone flow

on top of the sample compared to below the sample. The ozone flow is determined by the experimental

setup which has the ozone inlet installed at a sample height of 10 mm. The difference in oxide thickness

on the top and on the bottom is most pronounced if the sample is placed on the heater plate directly. The oxide on the bottom is very thin because the amount of ozone, which can get below the sample due to the not completely flat heater surface, is negligible. Unfortunately it is not possible to obtain an identical oxide thickness on both sides of the sample by growing oxides at the saturation thickness and then flipping them over and running another oxidation cycle at the same settings (refer also to the Appendix Section B.2).
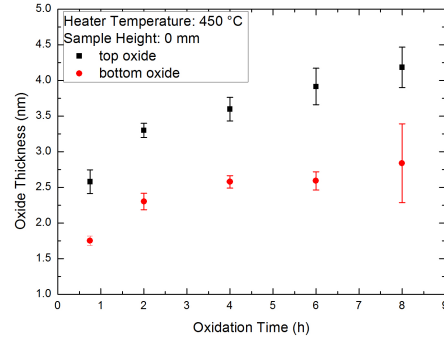
4.3.2 Temperature dependence

The temperature dependence of the oxide growth was studied, and the results are presented here. The samples were installed at different sample heights (10 mm or 0 mm above the heating plate), and then oxidized for 8 hours at different temperatures. We chose the oxidation time of 8 hours in order to run all experiments long enough to reach the saturation oxide thickness (compare to results of previous section). The oxide thickness was measured using spectroscopic ellipsometry. The saturation oxide thickness for different temperatures is shown in Figure 4.4. It can be seen that the saturation thickness strongly depends on the oxidation temperature. Thicker silicon oxides were observed for hi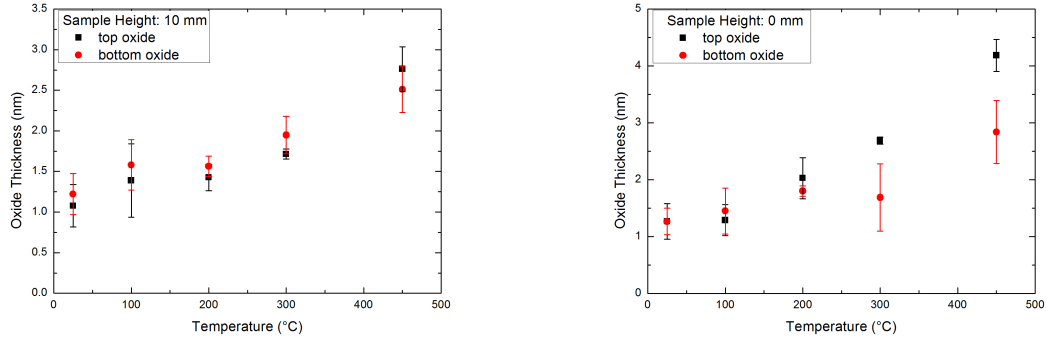gher temperatures. The increase in saturation oxide thickness for higher temperatures can be nicely seen on the top side of the sample. The saturation oxide thickness on the bottom side of the sample (which is facing the heating plate) also increases with temperature, but the oxide on the bottom is thin and there is a high variation of the thickness which can be observed from the large error bars. The reduced oxide thickness at the bottom can be explained by the lower availability of ozone at the bottom of the sample. The large variation of the oxide thickness at the bottom can be explained by the fact that ozone can only reach the sample due to inhomogeneities in the heating plate surface.

4.3.3 Additional considerations and remarks

1. In this section we showed the oxide thickness being dependent on the *heater* temperature and the sample height. These results can be used to plan the experimental parameters of the following passivation experiments. From a physical point of view the relation between oxide thickness and *sample* temperature is of interest. This information can be directly obtained by calculating the real sample temperature from the calibration curves in Figure 4.2(b).

2. The reported oxidation time always refers to the total ozone flow time. The total ozone flow time includes the time of ozone purging (15 min before the heater is turned on) and the temperature ramp time until the final temperature is reached (up to 25 minutes). Please also refer to the User

(a) Saturation oxide thickness at 0 mm sample height   (b) Saturation oxide thickness at 10 mm sample height

Figure 4.4: Temperature dependence of oxide growth. The saturation oxide thickness is shown for different temperatures at a sample height of 10 mm in a) or when placing the sample directly on the heating plate in b). The oxide thickness on the top side of the sample increases with increasing temperature. The thickness is quite homogeneous across the sample. The oxide on the bottom side of the sample is thinner and less homogeneous due to the limited availability of ozone. The saturation oxide thickness increases with temperature. The maximum thickness is higher when placing the sample directly on the heater surface due to the higher sample temperature.

Manual in the Appendix Section A.2 for more information on the total ozone flow time.

3. Additional experiments were performed in order to analyze the oxide growth and study the dependence on different parameters in detail. The results are presented in the Appendix B.

4.4   Surface passivation study

An extensive study was performed in order to find the best oxide parameters for the passivation of crystalline silicon using ozone-SiO_2 and PECVD-SiN_x. In this project, the effect of different oxide layers was investigated, while the conditions for the SiN_x depositions were kept constant. Samples with ozone oxide were prepared under a variety of different conditions. The samples were then coated with SiN_x using the optimal deposition conditions which had been found by by Chowdhury *et al* in previous experiments. The minority carrier lifetime was measured and the passivation quality was compared for different oxide parameters. Unless otherwise noted, the lifetime was measured using the Sinton lifetime tool, and the lifetime on both sides of the samples was averaged. Each data point represents one sample, and the error bar corresponds to the lifetime variation on the two sides of the sample.

4.4.1   Temperature dependence of passivation quality

Samples were oxidized for 8 h at different heater temperatures. The minority carrier lifetime was measured and compared. The lifetime for different oxidation temperatures is shown in Figure 4.5(a). We observe a strong decrease of minority carrier lifetime for silicon oxide layers which were grown at higher temperatures. The samples at 10 mm sample height always show higher lifetimes than the samples at 0 mm sample height. Re-oxidized samples show the worst surface passivation quality. We can extract the relation between the minority carrier lifetime and the silicon oxide layer thickness from the same data, since the saturation oxide thickness is directly related to the oxidation temperature. The saturation oxide thickness for different temperatures can be calculated from the results of Section 4.3.2. In Figure 4.5(b) the lifetime is compared for different oxide thicknesses. We observe a decrease in minority carrier lifetime for thicker silicon oxide layers. By comparison of both graphs in Figure 4.5, we can conclude that the highest lifetimes are obtained for 1.5 nm oxides grown at room temperature. Unfortunately, the oxidation temperature and the oxide thickness are directly related, and we cannot find out whether the oxidation temperature or the oxide thickness is the limiting factor for the minority carrier lifetime.

(a) Lifetime dependence on oxidation temperature   (b) Lifetime dependence on oxide thickness
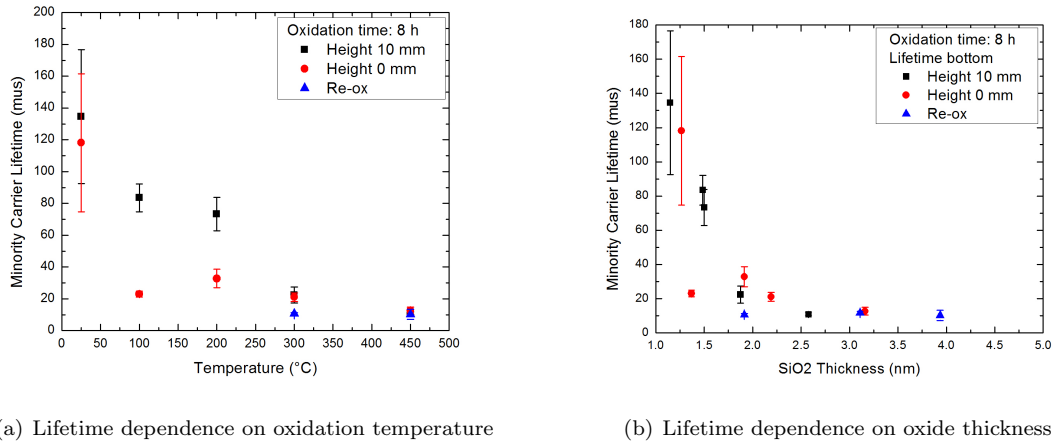
Figure 4.5: Temperature dependence carrier lifetime. Samples were oxidized for 8 h at different temperatures. The different oxidation temperature is directly related to the saturation oxide thickness. Minority carrier lifetime is shown in dependence on the oxidation temperature in a) and in dependence on the saturation oxide thickness in b). The data has been obtained from the same samples. The highest lifetimes can be obtained for a very thin oxide layer grown at room temperature.

4.4.2   Time dependence of passivation quality

Samples were oxidized at 450 °C and 25 °C for different periods of time. The minority carrier lifetime was analyzed for its dependence on oxidation time as shown in Figure 4.6. The passivation quality for

all 450 °C samples is very low and suggests that it is not worthy of further investigation. We conclude
that room temperature oxidation should be used for future experiments albeit an optimal temperature
may lie at an intermediate value between the extremes investigates here. The passivation quality for 25
°C samples shows a decrease for longer oxidation times. This is an interesting trend and will be further
analyzed in the next section.
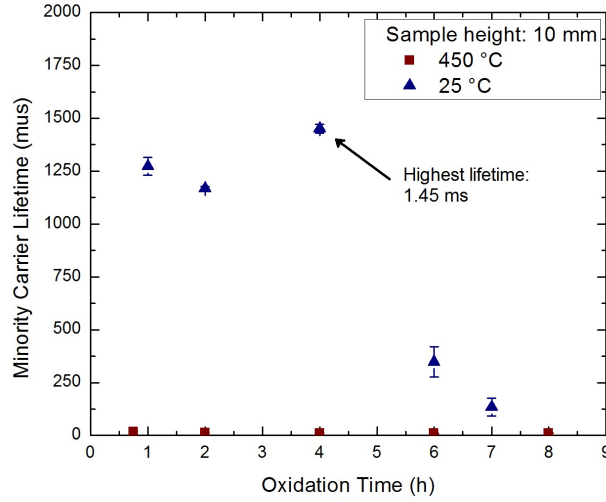
Figure 4.6: Lifetime in dependence on oxidation time at 450 °C (red) and at room temperature (blue).
Oxide layers grown at 450 °C show very low lifetimes < 200 μs. Oxide layers grown at room temperatures
show very high lifetimes up to 1465 μs. The lifetime decreases for longer oxidation times.

4.4.3   Detailed analysis of room temperature samples

In the previous section, we found that the minority carrier lifetime for room temperature samples de-
creases with oxidation time as shown in Figure 4.6. This trend cannot be explained by the oxide thickness
which already saturates after 45 minutes of ozone exposure as shown in Figure 4.3 in the section on ozone
oxide growth.

SE analysis and interface parameters

From the SE analysis, we can extract the refractive index of the oxide layer. Figure 4.7(a) shows that the refractive index is constant for different oxidation times. There is a variation of the SiN_x thickness as shown in Figure 4.7(b) but the nitride thickness variation has no correlation with the lifetime trend.

(a) Refractive index

(b) Silicon nitride thickness

(c) Silicon nitride SE parameters

(d) Interface parameters
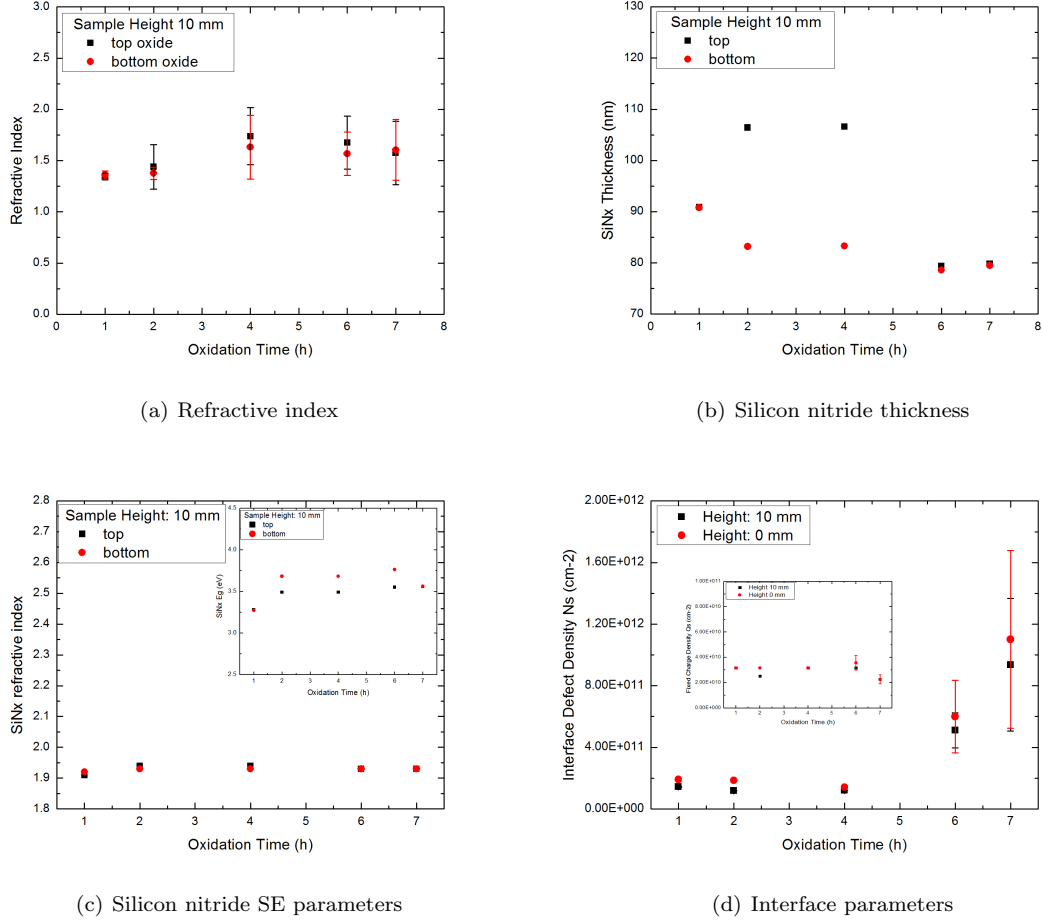
Figure 4.7: Detailed analysis of passivation quality using ozone oxide grown at room temperature. a) The refractive index of the silicon oxide is similar for all samples. It can not explain the dramatic change in lifetime for different samples. b) There is a variation of SiN_x thickness but the variation in thickness shows no correlation with the change in lifetime c) The refractive index is constant for all samples and the Tauc-gap (see inset) only shows small variations. d) The interface defect density is much higher for the low lifetime samples, which is in agreement with the higher surface recombination velocity. Inset: the fixed charge density is constant for all samples.

Based on two arguments, we assume that the variation of nitride thickness does not influence the passivation quality: 1) Previous results have shown that the passivation quality does not depend on the nitride thickness as long as it is thicker than 20 nm and 2) we compared the SiN_x properties by analyzing the refractive index and the Tauc-gap as shown in Figure 4.7(c), and found similar properties of the

silicon nitride film for all samples. For more detailed analysis, the defect density N_s and the fixed charge density Q_s were extracted from the interface recombination model. The results are shown in Figure 4.7(d). We observe that there is a strong increase in interface defect density N_s for the samples with lower ozone exposure. The higher defect density shows an excellent correlation with the lower lifetime of the samples. The fixed charge density Q_s at the interface is similar for all samples as shown in the inset. The findings from the interface recombination model are in agreement with the lifetime data, but the reason for the high defect density cannot be extracted from the interface recombination model itself.

Semilab analysis

In order to explain the decreasing lifetime for long oxidation times, the spatial distributions of the lifetimes were compared using the Semilab μPCD tool. The results are shown in Figure 4.8. Each graph shows two 1/4 wafer samples. The sample on the left was installed at 10 mm above the heating plate, while the sample on the right was placed directly on the heating plate.

(a) Oxidation for 1 h   (b) Oxidation for 2 h   (c) Oxidation for 4 h

(d) Oxidation for 6 h   (e) Oxidation for 7 h
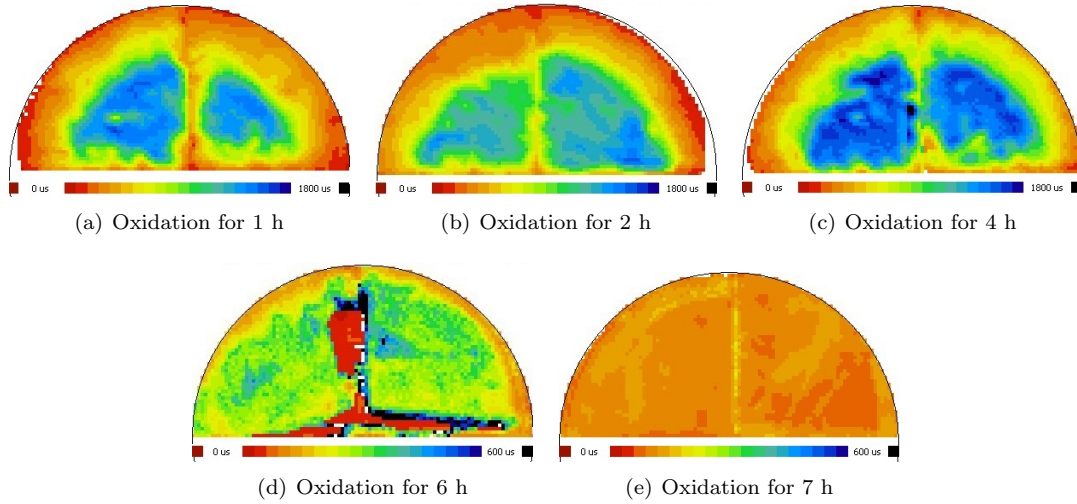
Figure 4.8: Spatial distribution of lifetime for room temperature samples. The lifetimes were measured on the top side of the sample. Each graph shows two samples with a size of 1/4 wafer. The sample on the left was installed at 10 mm above the heating plate, while the sample on the right was placed directly on the heating plate. High lifetimes are obtained for the samples from 1, 2 and 4 hour oxide growth. Low lifetimes are measured for 6 and 7 hour oxide growth. The spatial distribution of the high lifetime samples show higher lifetimes in the center and lower lifetimes near the edges, which is characteristic for all samples. The lifetime distribution of the low lifetime samples in d) is very inhomogeneous and may indicate that the low lifetimes are caused by shipping or handling inadequacies. Please note that the scale is adjusted for each graph in order to visualize the distribution of the lifetime.

The decrease in passivation quality for longer oxidation times, which was observed by the Sinton lifetime measurement, is confirmed by the Semilab lifetime data. Additionally, we observe from the spatial distributions that there are unusual variations of the minority carrier lifetime across the 6 hours ozone

oxidation samples as shown in Figure 4.8(d). There are large areas with almost no surface passivation. The 7 hours ozone oxidation samples (Figure 4.8(e)) show very low lifetimes all across the samples. We suggest that the low lifetimes can be associated with shipping or handling inadequacies during the silicon nitride depositions. This explanation seems reasonable, since all 4 samples with the low lifetimes were shipped in one box and coated with silicon nitride simultaneously. Future investigation is needed to support our assumption and to fully understand the phenomenon.

4.4.4   Comparison of wafer types and oxidation methods

The passivation study, presented in the previous sections, was done using standard SEMI quality n-type CZ wafers. The oxide layers were grown in our custom-built ozone oxidation chamber. In this section we present a few additional experiments in order to compare the results of our passivation study to other passivation schemes.

- Comparison of wafer types I: n-type CZ wafers, p-type CZ wafers, and n-type FZ wafers were compared using native oxide passivation (as proposed by Chowdhury *et al* [26])

- Comparison of wafer types II: n-type CZ wafers, p-type CZ wafers, and n-type FZ wafers were compared using 'UV-ozone' passivation ('UV-ozone' refers to an oxidation using a UVOCS Model T0606B UV/ozone cleaning system)

- Comparison of oxidation methods: native oxide passivation, UV-ozone passivation, and 'ozone' passivation was compared using n-type CZ wafers ('ozone' refers to an oxidation using our custom-built ozone oxidation chamber)

The size of the samples was one quadrant of a 4 inch diameter wafer. Ozone samples were HF etched and then oxidized using the given oxidation method for 1 h at room temperature. As-received wafers were used as native oxide samples. All samples were coated with an identical silicon nitride layer before the minority carrier lifetime was measured using Sinton lifetime tool. The passivation quality is shown in Table 4.1. Please note that the surface recombination velocity (SRV) is more expressive than the minority carrier lifetime when different sample thicknesses are compared.

From the comparison of wafer types and oxidation methods we can draw the following conclusions:

1. SiN_x passivation is not suitable for p-type wafers as shown in experiment #1 and #2. This finding will be discussed in more detail in the following section.

2. Better surface passivation is achieved using FZ wafers instead of CZ wafers when using identical passivation conditions (compare the results of #3 and #5, or the results of #4 and #6).

#	Type	Doping	Resistivity	Thickness	Oxide	Lifetime	SRV
1	CZ	p	15 Ωcm	500 μm	native	49 μs	510 cm/s
2	CZ	p	15 Ωcm	500 μm	UV-ozone	195 μs	128 cm/s
3	CZ	n	15 Ωcm	500 μm	native	342 μs	73 cm/s
4	CZ	n	15 Ωcm	500 μm	UV-ozone	868 μs	29 cm/s
5	FZ	n	1 Ωcm	280 μm	native	1027 μs	13.6 cm/s
6	FZ	n	1 Ωcm	280 μm	UV-ozone	1001 μs	14.0 cm/s
7	CZ	n	15 Ωcm	500 μm	ozone	1273 μs	19.6 cm/s

Table 4.1: Comparison of wafer types and oxidation methods. The lowest surface recombination velocities are measured for high quality FZ wafers using native oxide or UV-ozone oxide (#5 and #6). The SRV of standard CZ wafers using ozone oxide (#7) is much lower than the SRV of identical wafers using native oxide or UV-ozone oxide passivation. This result makes our custom-built ozone oxidation chamber a promising approach for surface passivation.

3. Much better surface passivation is achieved with our novel ozone oxide when compared to native oxide or UV-ozone oxide (compare the results of #3 and #4 to the results of #7). This result can be explained by the fact that our custom-built oxidation chamber provides a clean ozone-in-oxygen environment for the oxidation, whereas native oxide growth and the UV-ozone oxidation take place under 'dirty' atmospheric conditions.

In conclusion, we observed a very high lifetime and low a SRV using our ozone oxide passivation scheme for n-type CZ wafers. We expect to achieve even higher lifetimes, when using a full wafer instead of 1/4 wafer samples, because the edges of a sample are always responsible for lower lifetimes (as can be seen from the Semilab spatial distribution graphs). The results from this section allow us to assume a surface passivation comparable to previous results or even higher by using ozone oxide for full FZ wafers.

4.4.5 Theoretical explanation of SiNx passivation

The underlying effect which is responsible for surface passivation is not completely understood. For silicon nitride passivation, we assume that the passivation quality is based on a combination of two effects: 1) hydrogen diffuses through the thin silicon oxide layer and successfully passivates dangling bonds, and 2) fixed positive charges in the silicon nitride layer repel the holes from the surface. The field effect passivation due to the trapped positive charges is efficient for n-type silicon because the holes, which are minority carriers in n-type silicon, are kept away from the recombination centers at the surface. In p-type silicon, it is not important to keep the holes away from the recombination centers, because holes are majority carriers. The positive charges in the nitride film do not only repel the holes, but they also attract the electrons. The electrons, which are the important minority carriers in p-type silicon, are then lost due to recombination at the surface. Fixed positive charges at the surface of p-type silicon therefore increase the recombination rate. The repulsion of holes and attraction of electrons is

a positive effect for the surface passivation of n-type silicon, and a negative effect for the passivation of p-type silicon. From the comparison of wafer types in the previous section we found that the silicon nitride passivation scheme is not suitable for p-type wafers. This result is in perfect agreement with our theoretical explanation of SiN_x passivation.

4.4.6 Summary of passivation study

In conclusion we have found that low oxidation temperatures and low oxide thicknesses are favourable for surface passivation. The passivation quality decreases with temperature and with increasing oxide thickness. All oxide layers were thicker than 1 nm in our experiments due to the fast oxide growth at the beginning of the oxidation. Chowdhury *et al* have previously analyzed the dependence of the passivation quality for native oxide (which is always thinner than 1 nm). They have found that the passivation quality increases with the oxide thickness. Combining the two studies we propose that 1 nm of oxide grown at room temperature is a sweet spot for surface passivation. We found minority carrier lifetimes as high as 1450 μs for standard SEMI quality CZ wafers with a thickness of 500 μm. The lifetime corresponds to a surface recombination velocity of 17.2 cm/s. We expect to reach even higher lifetimes when using full high quality FZ wafers. We anticipate to achieve surface passivation which is comparable to state-of-the-art surface passivation schemes. Based on all low-temperature processes our ozone-SiO_2/PECVD-SiN_x passivation scheme constitutes an attractive alternative to common high temperature passivation.

4.5 Layer and interface characterization

The SiO_2 and the SiN_x films were characterized using spectroscopic ellipsometry. The SiO_2 layer was additionally analyzed using angle-resolved XPS and FT-IR. In this section we present additional information about the SiO_2 and SiN_x layers which has not been discussed in the preceding analysis.

4.5.1 SE analysis of SiNx layer

The SE data of the PECVD SiN_x layer can be fitted using the Tauc-Lorentz dielectric function model. There are 6 fitting parameters: SiN_x thickness, Tauc gap E_g, $\epsilon_1(\infty)$ parameter, peak 1 parameter A_0, peak 1 parameter E_0, peak 1 parameter C. In the fitting we set $\epsilon_1(\infty) = 1$ as suggested by other publications [30]. The obtained fitting parameters are shown in Table 4.2. The variation in Table 4.2 represents the range of parameters for different samples. The parameters for one separate sample were

Parameter	Measurement	Variation
Thickness	85 nm	± 15.0
E_g	3.6 eV	± 0.3
A_0	80 eV	± 15.0
E_0	10 eV	± 2

Table 4.2: SE parameters of SiN_x layer. The SiN_x layer thickness shows a significant variation for different samples. The Tauc gap E_g is similar for all samples, indicating comparable material properties.

obtained with a deviation of <5 % (apart from the peak 1 parameter C which was obtained with a deviation of >100 % and is not considered for the analysis). The refractive index n was found to be 1.95 ± 0.05 at a wavelength of 630 nm. From the SE analysis, only the layer thickness, the Tauc gap, and the refractive index have a direct physical meaning. We conclude that the SiN_x composition is similar for different depositions since the refractive index and the Tauc gap E_g are similar for all measurements. The SiN_x layer thickness varied significantly for different samples although the same recipe was used for every deposition. The change in deposition rate can be explained by a small variation in chamber temperature, since the PECVD system at the University of Western Ontario is not designed for temperatures > 350 °C. We chose to do the depositions at 400 °C (despite the varying deposition rate), because previous results by Chowdhury *et al* showed that the passivation quality was not sensitive to variations of the SiN_x layer thickness, but there was a strong dependence of the passivation quality on the PECVD temperature.

4.5.2 SE analysis of SiO₂ layer

The SE data of the ozone grown SiO_2 can be fitted using the Sellmeier S2 dielectric function model. There are 3 fitting parameters: SiO_2 thickness, UV parameter A, and UV parameter B. We have found that A was of the order of 1.5 ± 0.3 for all samples. The UV parameter B of all samples was found to be < 0.1 with a large deviation. There is no physical meaning associated with the fitting parameters which is why we do not further analyze them. During the native oxide growth, we measured values much larger than the refractive index of $n = 1.5$ for bulk SiO_2. We found that the refractive index of the SiO_x layer changes for ultra-thin oxide layers with a thickness of <1 nm, and it stays constant for oxide layers with a thickness of >1 nm. The data is shown in Figure 4.9. The change in refractive index is an interesting observation. However, there is no evidence that the refractive index analysis of the SE measurementis reliable for oxide films with <1 nm thickness. At this time we cannot decide whether it is a physical property or just a fitting error.
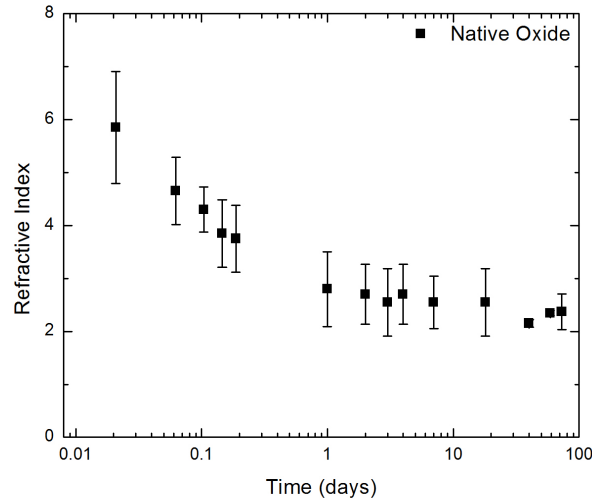
Figure 4.9: Native oxide refractive index. The measured refractive index during the first days of the native oxide growth is much higher than the bulk refractive index of SiO_2. The refractive index decreases as the native oxide grows back.

4.5.3   Angle-resolved XPS analysis of SiO₂ layer

Angle-resolved XPS can be used to calculate the thickness of the SiO_2 layer as explained in Section 2.5.2. Besides the layer thickness, we can obtain additional information from the $Si2_p$ data. The photoelectrons which are measured at high angles are related to the surface of the material, while the photoelectrons which are measured at low angles come from a region near the Si/SiO_2 interface. The $Si2_p$ data at an angle of 78° is shown in Figure 4.5.3. Between the elemental silicon peak and the silicon oxide peak, there is clear evidence of additional peaks which can be related to the existence of sub-oxides at the surface. The sub-oxide signal at the surface proves that angle-resolved XPS can be used to detect sub-oxides. At low angles we did not observe any sub-oxide peaks. We conclude that the existence of sub-oxides at the Si/SiO_2 interface is negligible and we have a high interface quality.
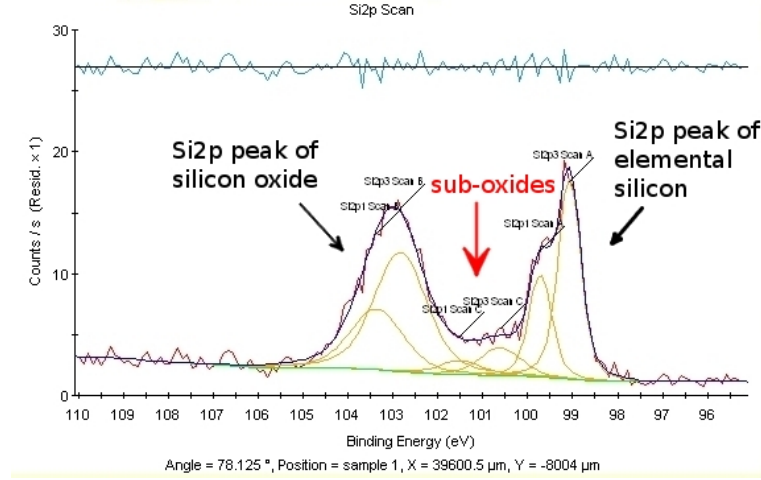
Figure 4.10: Sub-oxides at the surface of a silicon oxide layer. The Si2$_p$ data at 78° clearly shows additional peaks between the elemental silicon peak and the silicon dioxide peak. The intermediate energies can be related to the existence of sub-oxides at the surface.

4.5.4   FT-IR analysis of SiO₂ layer

FT-IR can be used to analyze the SiO$_2$ layer by measuring the frequency of the TO phonon peak of Si-O-Si asymmetric stretching vibration. IR absorption spectra of a sample were measured and then subtracted from a reference silicon sample. In this section we present the IR absorption both for the native oxide growth and for ozone oxide samples.

Native oxide

A 2 x 1 cm^2 FZ silicon sample was dipped in 2 % HF for 5 min. IR absorption spectra were measured during the native oxide growth. A sample with a saturated native oxide layer from the same silicon wafer was used as a reference. Using a native oxide sample as a reference instead of an oxide-free reference sample facilitates the experiment because it does not require HF etching before every measurement. The measured signal is the difference between the growing native oxide and the saturated native oxide. The results are shown in Figure 4.11. The first measurement was done directly after the etching procedure. We observed the expected decrease of the signal as the native oxide grew back with time. The measured absorption signal is very weak ($< 1\%$). The peak frequency in the first 6 days shows a shift in resonance frequency by only 1.1 cm^{-1} which implies that there are no big changes within the oxide structure. The peak frequency of 1059.5 cm^{-1} is low compared to the peak frequency of 1078.5 cm^{-1} for relaxed bulk silicon oxide [47]. The redshift can be related to strained bond angles or the existence of sub-oxides as explained in the Appendix Section C. We conclude that the oxide structure of the first native oxide layers differs from relaxed silicon oxide.
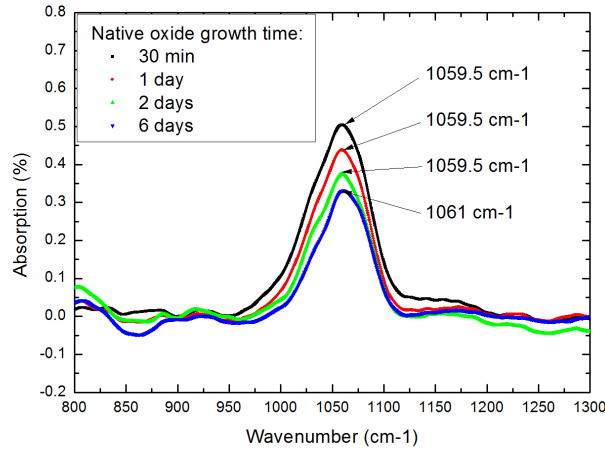
Figure 4.11: FT-IR peaks of native oxide. The peak at 1065 cm^{-1} is related to the TO phonon peak of the Si-O-Si asymmetric stretching vibration. The magnitude of the peak changes during the native oxide growth while the peak position remains constant.

Ozone oxide

Different 2 x 1 cm^2 FZ silicon samples were dipped in 2 % HF for 5 min and then oxidized in ozone under different conditions. IR absorption spectra were then measured using an oxide-free reference sample. The results are shown in Figure 4.12. We observed stronger signals for thicker oxides. Samples which had been oxidized at a sample height of 10 mm in Figure 4.12(a) show a change in resonance frequency from 1054 cm^{-1} to 1073 cm^{-1}. The redshift can be explained by structural differences compared to relaxed silicon oxide. The peak frequency of thicker oxides approaches the value of 1078.5 cm^{-1} for relaxed bulk silicon oxide which implies that the structural differences mainly exist in the first very thin oxide layers. Samples which had been oxidized directly on the heating plate show no change in peak frequency for two different oxide thicknesses as shown in Figure 4.12(b). The observed peak frequency of 1064 cm^{-1} is considerably lower than the value for relaxed silicon oxide. We conclude that the ozone oxide grown at high temperatures directly on the heating plate differs from relaxed silicon oxide. The structural difference of the sample which was oxidized directly on the heating plate is not restricted to the first oxide layers.

(a) FT-IR peaks at 10 mm sample height

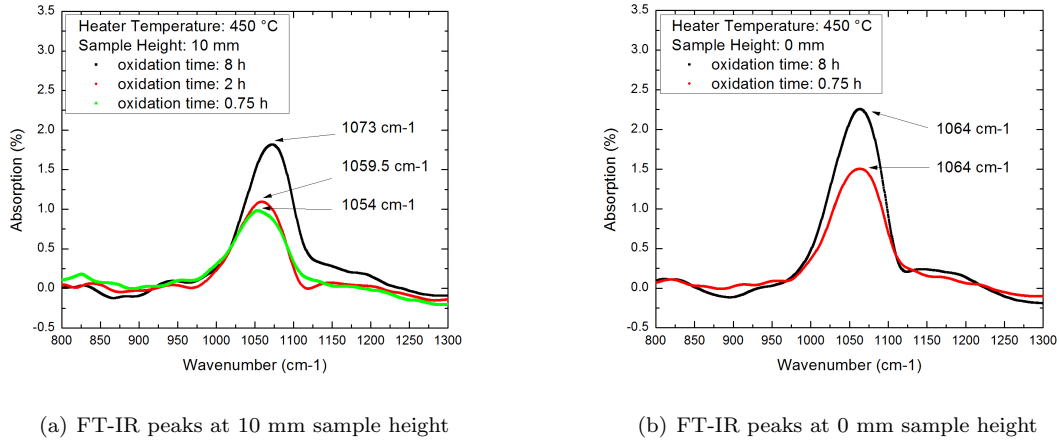(b) FT-IR peaks at 0 mm sample height

Figure 4.12: FT-IR peaks of ozone oxide grown at a heater temperature of 450 °C. a) The samples were installed at a sample height of 10 mm. The absorption frequency changes with the oxide thickness and approaches the value for relaxed silicon oxide. b) The samples were placed on the heating plate directly. The absorption frequency is low compared to relaxed silicon oxide.

FT-IR analysis summary

The above results show that we can successfully measure the TO phonon peak of Si-O-Si asymmetric stretching vibration for different oxide types. The signal magnitude depends on the oxide thickness. We have found different absorption frequencies for different samples. The first experiments which are presented here are a proof of principle demonstration. At this point we do not have enough data to correlate the FT-IR measurements to the passivation quality. An extensive study in the future will allow us to calculate the Si-O bond length and the bond angle for different oxides. The information about the oxide quality will contribute to a complete understanding of the results of the passivation study.

4.6 Surface Reflection Calculation

In order to design high-efficiency solar cells, not only the surface passivation is important, but also the surface reflection is a critical parameter. The total reflected energy by our bilayer passivation scheme was calculated using the theory for bilayer anti-reflection coatings as described in Section 2.2.4. We used the layers crystalline silicon (n = 3.5), silicon oxide (n = 1.5), silicon nitride (n = 2.0), and air (n = 1.0) for the calculation. The code was written in Fortran95 and the 3D graphs were plotted using gnuplot. The results are shown in Figure 4.13. The reflection depends on the SiO_2 layer thickness, the SiN_x layer thickness, and the wavelength of the incident light. Figure 4.13(a) shows that the minimum of reflection changes for different layer thicknesses. By integration the reflectivity over the solar irradiation we obtain

the total reflected energy. The total reflected energy depends on the SiO_2 and the SiN_x layer thickness as shown in Figure 4.13(b). From the reflection calculation we can see that we have a surface reflectivity as low as <5 % when using 85 nm SiN_x and <10 nm SiO_2 for surface passivation. The surface reflectivity of our bilayer passivation scheme is much lower than the surface reflectivity of 33 % for pure silicon. We conclude that our bilayer passivation scheme does not only enable excellent surface passivation, but also constitutes an efficient anti-reflection coating.
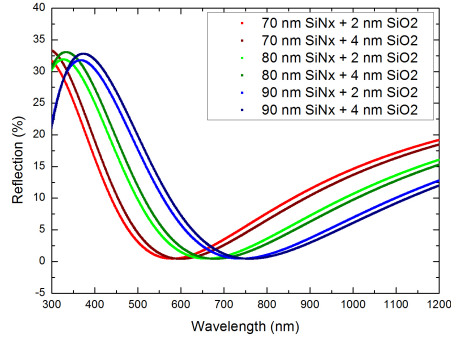
(a) Reflection depending on wavelength   (b) Total reflected energy
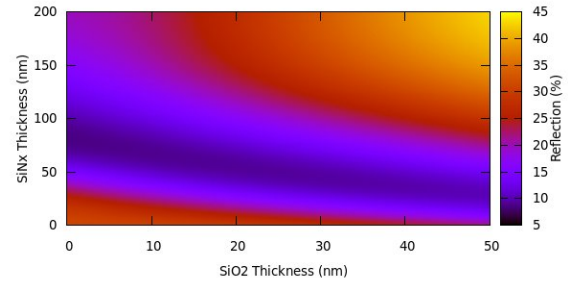
Figure 4.13: Surface reflection calculation. a) Reflected energy depending on the wavelength of incident light for different layer thicknesses. The results of a) are integrated over the solar irradiance to obtain the total reflected energy which is shown in b). For photovoltaic devices the layer thicknesses should be chosen according to the lowest reflectivity which correspondents to the dark blue region. A total reflected energy of <5 % can be achieved using our novel bilayer passivation scheme.

Chapter 5

Conclusion and Outlook

5.1 Conclusion

In this project, we showed that oxidation in ozone is a fast and elegant way to grow ultra-thin silicon oxide films which can be used for passivation of crystalline silicon. An extensive study identified the optimal oxidation conditions for passivation purposes. The results were evaluated in the context of high-efficiency photovoltaics. The main outcomes of this research are summarized here.

- A new oxidation chamber was designed. The experimental setup enables the oxidation of silicon in an ozone in oxygen atmosphere at temperatures up to 450 °C. Silicon oxide films of 1-5 nm thickness can be grown in less than 8 hours. The growth characteristics of the ozone oxide were analyzed under varying oxidation conditions.

- A novel low temperature passivation scheme for the surface of crystalline silicon was introduced. The passivation scheme consists of a bilayer of ultra-thin ozone-SiO_2 and 85 nm PECVD-SiN_x.

- An extensive study was performed in order to analyze the dependence of the passivation quality on the oxide thickness and the oxidation conditions. The optimal oxidation conditions were identified while the SiN_x layer was kept constant. The best passivation quality was achieved using 1.5 nm of SiO_2 grown in ozone atmosphere for 4 hours at room temperature.

- An effective surface recombination velocity of 17.2 cm/s was measured for an n-type CZ wafer (15 Ωcm resistivity, 500 μm thickness). This is an excellent result for standard SEMI quality CZ wafers. We expect that the passivation quality will be comparable to record-breaking passivation methods when using high quality FZ wafers.

- Our bilayer coating constitutes an excellent anti-reflection coating as demonstrated in our surface reflection calculation.

Our surface passivation scheme is in perfect agreement with the requirements for ultra-thin high-efficiency photovoltaics using new device structures like the BACH cell. The low temperature processing of the passivation layers allows for the use of lower quality silicon as a substrate material. The facile production at low temperatures and the excellent surface passivation quality defines our results as an important step towards subsidy-free solar energy for everyone.

5.2   Future work

The results of this project allow to identify the optimal conditions for surface passivation. Future studies will focus on oxidation at room temperature or slightly elevated temperatures. A few questions were raised during the project and further experiments are needed for clarification.

- The relation between the oxide growth time and the passivation quality requires detailed analysis. The decrease of passivation quality for longer oxidation times at room temperature cannot be explained so far.

- We assume that diffusion of hydrogen through the silicon oxide layer is an important parameter for the passivation of dangling bonds. Aging of the silicon oxide film under different conditions (nitrogen, ozone, oxygen, argon, moisture) may have a significant influence on the passivation quality and detailed investigation is required.

- Further experiments are needed to test the surface passivation quality on different substrates: 1) high quality FZ wafers, and 2) low quality multi-crystalline wafers. Experiments on FZ wafers are needed to report the highest possible passivation quality using our novel passivation scheme. Experiments on multi-crystalline wafers are important because the use of lower quality materials will help to further reduce the solar cell cost. According to previous findings, the ozone oxide growth should be independent of the crystalline orientation.

- Up to now we have very little understanding with respect to the microscopic effects of our bilayer passivation scheme. The change in IR absorption and the values for the trapped charge density and the defect density obtained from the interface recombination model are the only indicators so far. Future experiments will include cross-sectional transmission electron microscopy (TEM) and medium energy ion spectroscopy (MEIS). Additional information about the structure can be

extracted from TEM images. MEIS measurements will allow us to probe the composition of the oxide layer and may bring interesting information (for example the formation of silicon oxynitrides).

The last big step will be to fabricate solar cells using our novel bilayer passivation scheme as surface passivation scheme for the crystalline silicon substrate. The reported surface passivation scheme is suitable for the fabrication of ultra-thin photovoltaic devices like the BACH cell which has been proposed by our group. The cell performance (short circuit current, open circuit voltage, fill factor) will give further insight into the topic.

5.3   Outlook

The availability and the price of fossil energy resources constantly changes due to political strategies as well as novel discoveries and exploitation technologies. The advances of renewable energies however should not only be driven by the fear to run out of energy. "The Stone Age didnt end for lack of stone, and the oil age will end long before the world runs out of oil." [1]

---

[1]Sheik Ahmed Zaki Yamani. New York Times, 2005

Bibliography

[1] BP. Statistical Review of World Energy, 2012. 1.1

[2] Vaclav Smil. *General Energetics: Energy in the Biosphere and Civilization.* John Wiley & Sons, 1991. 1.1

[3] Martin A. Green. *Solar Cells: Operating Principles, Technology, and System Applications.* Prentice Hall, 1981. 1.2.2

[4] Robert F. Pierret. *Advanced Semiconductor Fundamentals.* Addison-Wesley, 1987. 1.2.3

[5] Sadao Sakamoto and Toshimitsu Oshiro. Field Test Results on the Stability of Crystalline Silicon Photovoltaic Modules Manufactured in the 1990s. In *3rd World Conference on Photovoltaic Energy Conversion*, number V, 2003. 1.3.1

[6] J.R. Chelikowsky and L. Cohen. Electronic structure of silicon. *Physical Review B*, 10(12):5095, 1974. 1.2(a)

[7] C. Wehrli. Extraterrestrial Solar Spectrum. *Physikalisch-Meteorologisches Observatorium + World Radiation Center (PMO/WRC) Davos Dorf*, 615, 1985. 1.2(b), 2.2.4

[8] William Shockley and Hans J. Queisser. Detailed Balance Limit of Efficiency of p-n Junction Solar Cells. *Journal of Applied Physics*, 32(3):510, 1961. 1.3.2

[9] Martin A. Green, Keith Emery, Yoshihiro Hishikawa, Wilhelm Warta, and Ewan D Dunlop. Solar cell efficiency tables (version 40). *Progress in Photovoltaics: Research and Applications*, 20:606, 2012. 1.3.2

[10] Jianhua Zhao, Aihua Wang, Martin a. Green, and Francesca Ferrazza. 19.8% Efficient Honeycomb Textured Multicrystalline and 24.4% Monocrystalline Silicon Solar Cells. *Applied Physics Letters*, 73(14):1991, 1998. 1.3.2

[11] A. Upadhyaya, M. Sheoran, A. Ristow, A. Rohatg, S. Narayanan, and S. Roncin. Greater than 16thick cast multicrystalline silicon. In *Photovoltaic Energy Conversion, Conference Record of the 2006 IEEE 4th World Conference on*, volume 1, pages 1052–1055, 2006. 1.3

[12] Abdelazize Laades, Hans-Peter Sperlich, Mario Bähr, Uta Stürzebecher, Carlos a. Diaz Alvarez, Markus Burkhardt, Heike Angermann, Michael Blech, and Alexander Lawerenz. On the impact of interfacial SiOx-layer on the passivation properties of PECVD synthesized aluminum oxide. *Physica Status Solidi (C)*, 9, October 2012. 2.1.1

[13] S. C. Chao, R. Pitchai, and Y. H. Lee. Enhancement in Thermal Oxidation of Silicon by Ozone. *Journal of The Electrochemical Society*, 136(9):2751, 1989. 2.1.1

[14] K Hirose, H Nohira, K Azuma, and T Hattori. Photoelectron spectroscopy studies of SiO2/Si interfaces. *Progress in Surface Science*, 82:3–54, 2007. 2.1.2

[15] K. Nakamura and S. Ichimura. Vibrational Spectroscopic Study of the Interface of SiO2/Si(100) Fabricated by Highly Concentrated Ozone: Direct Evidence for Less Strained Si-O-Si Bond Angle. *Japanese Journal of Applied Physics*, 44(10):7602, October 2005. 2.1.2, C.2.1, D.2(b), D.3.2

[16] Mark J Kerr and Andres Cuevas. Recombination at the interface between silicon and stoichiometric plasma silicon nitride. *Semiconductor Science and Technology*, 17(2):166–172, February 2002. 2.2.1, 2.2.2

[17] Mikio Taguchi, Kunihiro Kawamoto, Sadaji Tsuge, Toshiaki Baba, and Hitoshi Sakata. HIT Cells - High Efficiency Crystalline Si Cells with Novel Structure. *Progress in Photovoltaics: Research and Applications*, 8, 2000. 2.2.2

[18] B. Hoex, S. B. S. Heil, E. Langereis, M. C. M. van de Sanden, and W. M. M. Kessels. Ultralow surface recombination of c-Si substrates passivated by plasma-assisted atomic layer deposited Al2O3. *Applied Physics Letters*, 89(4):042112, 2006. 2.2.2

[19] I. Martin, M. Vetter, A. Orpella, C. Voz, J. Puigdollers, and R. Alcubilla. Surface passivation of n-type crystalline Si by plasma-enhanced-chemical-vapor-deposited amorphous SiCx:H and amorphous SiCxNy:H films. *Applied Physics Letters*, 81(23):4461, 2002. 2.2.2

[20] G. Dingemans, M. M. Mandoc, S. Bordihn, M. C. M. van de Sanden, and W. M. M. Kessels. Effective passivation of Si surfaces by plasma deposited SiOx/a-SiNx:H stacks. *Applied Physics Letters*, 98:222102, 2011. 2.2.2

[21] Stefan Dauwe, Lutz Mittelstaedt, Axel Metz, and Rudolf Hezel. Experimental evidence of parasitic shunting in silicon nitride rear surface passivated solar cells. *Progress in Photovoltaics: Research and Applications*, 10(4):271–278, June 2002. 2.2.2

[22] Marc Hofmann, Stefan Janz, Christian Schmidt, Stephan Kambor, Dominik Suwito, Norbert Kohn, Jochen Rentsch, Ralf Preu, and Stefan W. Glunz. Recent developments in rear-surface passivation at Fraunhofer ISE. *Solar Energy Materials and Solar Cells*, 93(6-7):1074–1078, June 2009. 2.2.2

[23] Jan Schmidt, Mark Kerr, and Andres Cuevas. Surface passivation of silicon solar cells using plasma-enhanced chemical-vapour-deposited SiN films and thin thermal SiO2/plasma SiN stacks. *Semiconductor Science and Technology*, 16:164, 2001. 2.2.2

[24] Yevgeniya Larionova, Verena Mertens, Nils-Peter Harder, and Rolf Brendel. Surface passivation of n-type Czochralski silicon substrates by thermal-SiO2/plasma-enhanced chemical vapor deposition SiN stacks. *Applied Physics Letters*, 96(3):032105, 2010. 2.2.2

[25] S. Narasimha and a. Rohatgi. Effective passivation of the low resistivity silicon surface by a rapid thermal oxide/plasma silicon nitride stack. *Applied Physics Letters*, 72(15):1872, 1998. 2.2.2

[26] Zahidur R. Chowdhury, Kevin Cho, and Nazir P. Kherani. High-quality surface passivation of silicon using native oxide and silicon nitride layers. *Applied Physics Letters*, 101(2):021601, 2012. 2.2.3, 2.2(a), 3.1.3, 4.1, 4.4.4

[27] Z. Cui, J. M. Madsen, and C. G. Takoudis. Rapid thermal oxidation of silicon in ozone. *Journal of Applied Physics*, 87(11):8181, 2000. 2.2.3

[28] Hyo Sik Chang, Sangmoo Choi, Dae Won Moon, and Hyunsang Hwang. Improved Reliability Characteristics of Ultrathin SiO 2 Grown by Low Temperature Ozone Oxidation. *Japanese Journal of Applied Physics*, 41:597, October 2002. 2.2.3, D.3.3, D.3

[29] K. Koike, K. Izumi, S. Nakamura, G. Inoue, A. Kurokawa, and S. Ichimura. Synthesis of silicon dioxide film using high-concentration ozone and evaluation of the film quality. *Journal of Electronic Materials*, 34(3):240, March 2005. 2.2.3

[30] G.E. Jellison, F.A. Modine, P. Doshi, and A. Rohatgi. Spectroscopic ellipsometry characterization of thin-film silicon nitride. *Thin Solid Films*, 313-314:193–197, February 1998. 2.2.4, 2.5.1, 4.5.1

[31] B. A. Moys. The theory of double-layer antireflection coatings. *Thin Solid Films*, 21:145–157, 1974. 2.2.4

[32] John P. McKelvey. *Solid State and Semiconductor Physics*. Krieger Pub Co, 1982. 2.3

[33] Ronald a. Sinton and Andres Cuevas. Contactless determination of currentvoltage characteristics and minority-carrier lifetimes in semiconductors from quasi-steady-state photoconductance data. *Applied Physics Letters*, 69(17):2510, 1996. 2.3.1, 2.3.2

[34] Sara Olibet, Evelyne Vallat-Sauvain, and Christophe Ballif. Model for a-Si:H/c-Si interface recombination based on the amphoteric nature of silicon dangling bonds. *Physical Review B*, 76(3):1–14, July 2007. 2.4, 2.3

[35] Barzin Bahardoust, Alongkarn Chutinan, Keith Leong, Adel B. Gougam, Davit Yeghikyan, Tome Kosteski, Nazir P. Kherani, and Stefan Zukotynski. Passivation study of the amorphous-crystalline silicon interface formed using DC saddle-field glow discharge. *Physica Status Solidi (a)*, 207(3):539–543, March 2010. 2.4.2, 3.2.1

[36] Hiroyuki Fujiwara. *Spectroscopic Ellipsometry: Principles and Applications*. John Wiley & Sons, 2007. 2.5.1

[37] Yanyan Chen and Gang Jin. Refractive index and thickness analysis of natural silcion dioxide film growing on silicon with variable-angle spectroscopic ellipsometry. *Spectroscopy*, 10(21), 2006. 2.5.1

[38] A. R. Forouhi and I. Bloomer. Optical dispersion relation for amorphous semiconductors and amorphous dielectrics. *Physical Review B*, 34(10), 1986. 2.5.1

[39] G. E. Jellison and F. A. Modine. Parameterization of the optical functions of amorphous materials in the interband region. *Applied Physics Letters*, 69(3):371, 1996. 2.5.1, 2.5.1

[40] John F. Watts and John Wolstenholme. *Surface Analysis by XPS and AES*. John Wiley & Sons, 2003. 2.5.2, 2.4

[41] Environment Canada. Ambient Levels of Ground-Level Ozone, 2012. 3.1.2

[42] Plinio Innocenzi. Infrared spectroscopy of solgel derived silica-based films: a spectra-microstructure overview. *Journal of Non-Crystalline Solids*, 316:309–319, February 2003. 3.1.3

[43] Tydex. Materials for Transmission Optics: Silicon. 3.1.3

[44] C. Leendertz, N. Mingirulli, T. F. Schulze, J. P. Kleider, B. Rech, and L. Korte. Discerning passivation mechanisms at a-Si:H/c-Si interfaces by means of photoconductance measurements. *Applied Physics Letters*, 98(20):202108, 2011. 3.2.1

[45] I. H. Malitson. Interspecimen comparison of the refractive index of fused silica. *Journal of the Optical Society of America*, 55(10):1205–1208, Oct 1965. 3.2.2

[46] C. K. Fink, K. Nakamura, S. Ichimura, and S. J. Jenkins. Silicon oxidation by ozone. *Journal of physics: Condensed matter*, 21(18):183001, May 2009. 4.3.1, D.1, D.2, D.2.1, D.4, D.4

[47] J.T. Fitch, C.H. Bjorkman, G. Lucovsky, F.H. Pollak, and X. Yin. Local atomic structure at thermally grown si/sio2 interfaces. *Applied Surface Science*, 39(14):103 – 115, 1989. 4.5.4, C.2.1

[48] Feliciano Giustino and Alfredo Pasquarello. Infrared Spectra at Surfaces and Interfaces from First Principles: Evolution of the Spectra across the Si(100)-SiO2 Interface. *Physical Review Letters*, 95(18):187402, October 2005. C.2, C.1, C.2.2, C.3

[49] P. N. Sen and M.F. Thorpe. Phonons in AX2 glasses: From molecular to band-like modes. *Physical Review B*, 15, 1977. C.2.1

[50] Frank L Galeener. Band limits and the vibrational spectra of tetrahedral glasses. *Physical Review B*, 19(8), 1979. C.2

[51] Shunsuke Hosokawa and Shingo Ichimura. Ozone jet generator as an oxidizing reagent source for preparation of superconducting oxide thin film. *Review of Scientific Instruments*, 62(6):1614, 1991. D.1

[52] Kunihiko Koike, Tatsuo Fukuda, Shingo Ichimura, and Akira Kurokawa. High-concentration ozone generator for oxidation of silicon operating at atmospheric pressure. *Review of Scientific Instruments*, 71(11):4182, 2000. D.1

[53] Tetsuya Nishiguchi, Yoshiki Morikawa, Mitsuru Kekura, Masaharu Miyamoto, Hidehiko Nonaka, and Shingo Ichimura. Reactive oxygen beam generation system using pulsed laser evaporation of highly concentrated solid ozone. *Review of Scientific Instruments*, 73(3):1217, 2002. D.1

[54] A. Tosaka, T. Nishiguchi, H. Nonaka, and S. Ichimura. Low-Temperature Oxidation of Silicon using UV-Light-Excited Ozone. *Japanese Journal of Applied Physics*, 44(36):L1144, August 2005. D.1

[55] S. Ichimura, H. Nonaka, Y. Morikawa, T. Noyori, T. Nishiguchi, and M. Kekura. Development of a continuous generation/supply system of highly concentrated ozone gas for low-temperature oxidation process. *Journal of Vacuum Science & Technology A: Vacuum, Surfaces, and Films*, 22(4):1410, 2004. D.1

[56] T. Maeda, A. Kurokawa, K. Sakamoto, A. Ando, H. Itoh, and S. Ichimura. Atomic force microscopy observation of layer-by-layer growth of ultrathin silicon dioxide by ozone gas at room temperature. *Journal of Vacuum Science & Technology B: Microelectronics and Nanometer Structures*, 19(2):589, 2001. D.1

[57] N. Kameda, T. Nishiguchi, Y. Morikawa, M. Kekura, H. Nonaka, and S. Ichimura. High Quality Gate Dielectric Film on Poly-Silicon Grown at Room Temperature using UV Light Excited Ozone. *Journal of The Electrochemical Society*, 154(9):H769, 2007. D.2.2, D.1

[58] S Ichimura, A Kurokawa, K Nakamura, H Itoh, H Nonaka, and K Koike. Ultrathin SiO 2 film growth on Si by highly concentrated ozone. *Thin Solid Films*, 377:518–524, 2000. D.3.1, D.2(a)

[59] Christian Fink and Stephen Jenkins. First-principles molecular dynamics of the initial oxidation of Si{001} by ozone. *Physical Review B*, 78(19):195407, November 2008. D.4

Appendix A

Additional information:

Ozone Oxidation Chamber

A detailed list of the chamber parts and a user manual for ozone oxidation is given in this section.

A.1   Chamber parts

The following parts were used for the experimental setup in addition to the custom designed parts:

- A2Z Model 2GLAB ozone generator (A2Z Ozone)

- CN2110 temperature controller (Omega)

- Catalytic ozone destructor (Ozone Lab)

- CSH-103200/120V catridge heater (Omega)

- MMA-21 flowmeter (Dwyer)

- 1/4 inch tubes, valves and connectors (Swagelok)

- Silvertronic stainless steel alligator clips (Newark)

- Type K thermocouple feedthrough with CF flange (Kurt J. Lesker Company)

- Power feedthrough with CF flange (Kurt J. Lesker Company)

- CF half nipples (Kurt J. Lesker Company)

A.2   User manual

System start and oxidation

1. Install samples inside chamber. Use appropriate holders to chose the sample height above the heating plate:

   - alligator clips: 1 cm

   - ceramic pearls: 3 mm

   - directly on heater: 0 mm

2. Close and lock chamber. Ensure that all gas lines are properly connected and all valves are closed.

3. Open main valve of the oxygen bottle and adjust pressure to 10 PSI.

4. Open the gas flow valve at the oxygen bottle and regulate the oxygen flow to 4 L/min on the flowmeter of the ozone generator.

5. Purge chamber with oxygen for 5 min.

6. Start ozone generator and ensure that the ozone concentration is set to 100 %.

7. Purge chamber with ozone in oxygen for 15 min.

8. Switch on temperature controller and set the desired temperature (refer to the calibration curve).

9. Decrease the gas flow to 2 L/min and oxidize for the desired time.

System shut down

1. Turn off the temperature controller or set temperature to 10 °C.

2. Turn off the ozone generator (main switch).

3. Purge the ozone generator and the system with oxygen at a flow of 4 L/min for 5 min.

4. Close all oxygen valves.

5. Open all argon valves and purge chamber with argon at a flow of 2.5 L/min for 30 min.

6. Wait until chamber and sample is cooled down below 50 °C.

7. Open chamber. If you can still smell ozone, immediately close the chamber again and continue purging with argon for at least 15 min.

Refer to suppliers manuals for detailed information on the ozone generator or the temperature controller.

Appendix B

Additional experiments: Ozone oxide growth

The main parameters of the ozone oxide growth are the oxidation temperature and the oxidation time which are discussed in the Results Section 4.3. Additional experiments were performed in order to analyze the oxide growth and study the dependence on different parameters in detail.

B.1 Homogeneity of oxidation

A rough estimate of the homogeneity of the oxide thickness can be extracted from all oxide growth graphs which are presented in the Results Section 4.3. The oxide thickness was always measured on 6 different sites across the sample. The average oxide thickness is presented as data point and the variation of the oxide thickness can be seen from the error bars. The homogeneity was analyzed in detail by comparing 3 different samples (1 x 1 cm^2) which were installed in different parts of the chamber at the same height. The oxide thickness was measured on two different sites on each side of the samples. The results are shown in Figure B.1. Every data point corresponds to a separate sample. The variation of the tow measurement sites can be obtained from the error bars. Similar oxide growth can be observed for all three samples. The variation of oxide thickness is within the error of measurement.
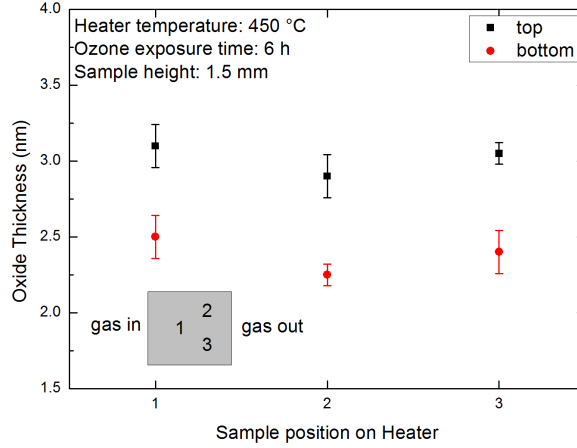
Figure B.1: Homogeneity of oxidation. a) Three 1 x 1 cm^2 samples were installed in different locations in the chamber. The inset shows the sample locations with respect to the heating plate (grey) and the gas in- and outlet. All three samples show a similar oxide growth.

B.2 Oxide growth on both sample sides

The gas inlet is fixed in the chamber at a height of 10 mm above the heater plate. The oxide thickness strongly depends on the availability of ozone. The oxide on the top of the sample is always thicker than on the bottom of the sample if the sample is installed at a height < 10 mm. A sample must be installed at a sample height of 10 mm in order to obtain homogeneous oxide thicknesses on both sides of the sample. However, only oxides up to 2.5 nm thickness can be grown at the sample height of 10 mm due to the lower sample temperature. We are interested in homogeneous oxides thicker than 2.5 nm, and studied the effect of re-oxidation. Samples which were oxidized on both sides on the sample in two subsequent oxidation cycles using the same parameters. The variable parameter in those experiments is the sample temperature and not the oxidation time because a homogeneous oxide thickness can only be obtained if the cycles are run long enough to saturate the oxide growth at a certain temperature. Samples were one quadrant of a 4 inch diameter n-type CZ wafer with 15 Ωcm resistivity. The samples were placed directly on the heater surface and oxidized for 8 h at 450 °C and 300 °C respectively. The thickness both on the top side (Side 1) and the bottom side (Side 2) after the first oxidation was measured. The samples were then flipped over and re-oxidized under the same conditions. In the second oxidation Side 2 is facing up. The oxide thickness on both sides is shown in Table B.1 after the first and after the second oxidation.

After the second oxidation, we expected the samples to have a similar oxide layer on both sides of the sample. However, when we compared the measurements after the second oxidation to the measurements

#	Temperature	Oxide Thickness			
		1st oxidation		2nd oxidation	
		Side 1	Side 2	Side 1	Side 2
1	450 °C	4.3±0.9 nm	2.9±0.2 nm	4.2 ±0.2 nm	3.6±0.3 nm
2	300 °C	2.6±0.1 nm	2.1±0.3 nm	1.8±0.1 nm	2.0±0.4 nm

Table B.1: Oxide growth on both sample sides. The oxide thickness is measured on the top side (Side 1) and on the bottom side (Side 2) after the first oxidation. The samples are then flipped over (Side 1 is now the bottom side) and the oxidation is repeated using the same parameters. The resulting oxide thickness is not homogeneous.

after the first oxidation we found that the oxide thickness was not homogeneous and sometimes even smaller than after the first oxidation. We conclude that it is not possible to prepare samples with an equally thick oxide layer > 2.5 nm on both sides of the sample using this approach. Future experiments are needed in order to find an explanation for the observed results.

B.3   Reproducibility

Samples were prepared under identical conditions in two different oxidation experiments in order to prove the reproducibility of the ozone oxide growth. The results are shown in Table B.2. Similar oxide growth was obtained for samples which were oxidized under the same conditions. The variation of oxide thickness for different experiment is within the measurement error. We conclude that we can grow reproducible oxide films using our custom-built ozone oxidation chamber.

#	Oxidation conditions			Oxide Thickness			
	Temperature	Time	Height	Sample 1		Sample 2	
				top	bottom	top	bottom
1	450 °C	8 h	10 mm	2.8±0.3 nm	2.5±0.3 nm	2.6±0.1 nm	2.6±0.1 nm
1	450 °C	8 h	0 mm	4.2±0.3 nm	2.8±0.6 nm	3.8±0.3 nm	2.5±0.1 nm
1	300 °C	8 h	10 mm	1.7±0.1 nm	2.0±0.2 nm	1.9±0.1 nm	1.8±0.1 nm

Table B.2: Reproducibility of oxide growth. Samples were oxidized under identical conditions in order to prove the reproducibility of the ozone oxide growth. The oxide thickness for different samples is similar within the measurement error.

B.4   Absence of ozone or absence of heating

Two control experiments were performed to prove the necessity of both ozone and heating in order to grow oxide films with >1.5 nm thickness. 1) Samples were oxidized at 450 °C in a 100 % oxygen atmosphere (without ozone). 2) Samples were oxidized at room temperature in a 1 % ozone atmosphere without heating. The results are shown in Figure B.2. We observed a saturation of the oxide growth at

the native oxide thickness, both at the absence of ozone, and at the absence of heating.
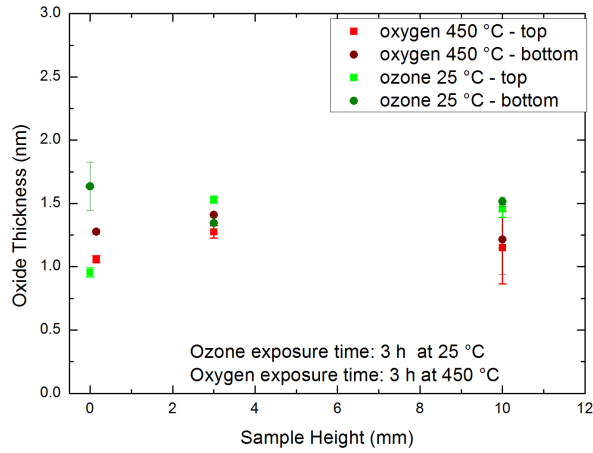

Figure B.2: Control experiments. Red: Samples were oxidized at 450 °C in a 100 % oxygen atmosphere (without ozone). Green: Samples were oxidized at room temperature in a 1 % ozone atmosphere without heating. Both experiments show that the oxide thickness after 3 hours does not exceed 1.5 nm which is comparable to the native oxide thickness.

B.5   Flow rate dependence

An additional experiment was performed to study the dependence of the oxide growth on the gas flow rate. Two sets of samples are compared. One set of samples was oxidized at a flow rate of 2 L/min and the other set of samples was oxidized at 4 L/min. Each set of samples consisted of 3 samples which were installed at a different height above the heater surface. The results are shown in Figure B.3. In contrast to our expectations, the oxide thickness showed no obvious dependence on the flow rate (the change in oxide thickness is within the measurement error). This result can be interpreted in two different ways: 1) the oxide thickness does not strongly depend on the ozone concentration, or 2) the ozone concentration inside the chamber is similar for higher and lower flow rates. The first explanation is unlikely, considering that no oxidation is observed at the absence of ozone (as discussed in the previous section). The second explanation implies that the decomposition of ozone, due to its limited lifetime inside the chamber, counteracts the effect of the presumably higher ozone concentration at low flow rates. Unfortunately, the ozone concentration in our setup is not exactly determined and therefore we are unable to specifically analyzed the influence of the ozone concentration until a precise ozone concentration detector will be purchased. The analysis could be interesting for future work.
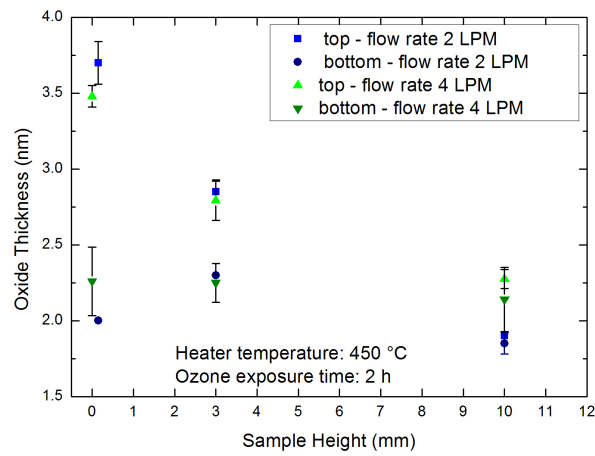
Figure B.3: Calibration of gas flow rate. Two sets of samples are compared. The first set of samples (blue) was oxdized at a gas flow of 2 L/min. The second set of samples (green) was oxidized at a gas flow of 4 L/min. The resulting oxide thickness is similar for both experiments.

Appendix C

Theoretical background: FT-IR characterization

Fourier-transform infrared spectroscopy (FT-IR) can be used to characterize the composition and the microscopic structure of a material. It has been used by several groups in order to analyze silicon oxide layers. The underlying principle and the experimental results are summarized here.

C.1 Fourier-transform infrared spectroscopy

FT-IR is a technique to measure the absorption of infrared light by a material. The sample is illuminated with a beam which is composed of different infrared frequencies, and the absorption of the material is measured. The beam is then modified to contain a different combination of frequencies and the measurement is repeated. In the end, all data is combined in order to calculate the absorption at every wavelength. Bending, stretching, and rocking vibrational motions can be excited in the sample. Those vibrations can be detected by measuring IR absorption because their energy is in the IR range. The vibrational modes are characteristic for the sample and depend on the elements, the bond lengths, and the bond orientations.

C.2 FT-IR characterization of SiO_2

Several groups have studied thin SiO_2 films on silicon using IR absorption. The experimental data revealed a redshift of the transverse and longitudinal Si-O stretching frequencies for decreasing oxide thicknesses as shown in Figure C.1. This redshift has variably been ascribed to compressive strain in the

interfacial oxide, to void incorporation, or to the sub-stoichiometric oxide (for details refer to Giustino *et al* [48]). Two possible explanations for the redshift are summarized below. In our experiments we measure the IR absorption frequency in order to analyze the redshift of the peak frequency. However we do not have enough data in order to relate the origin of the redshift to one of the models.
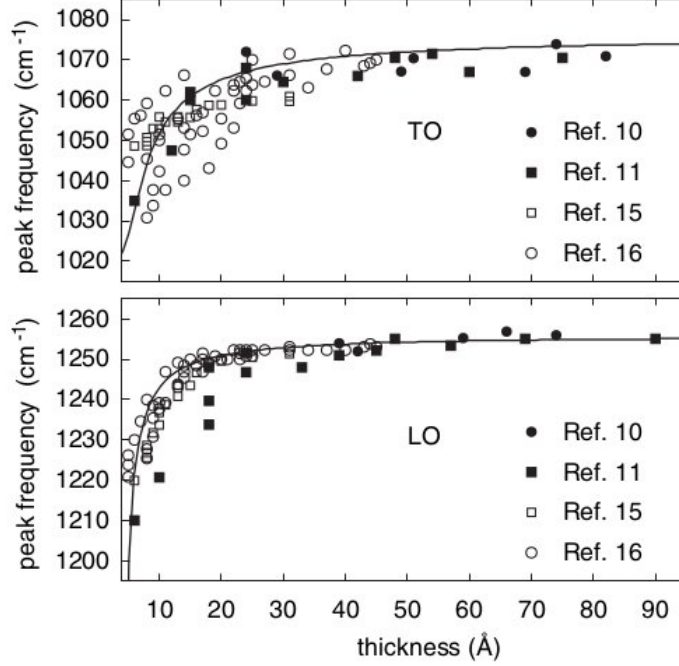

Figure C.1: Redshift of IR absorption for decreasing SiO_2 thickness. Experimental results from different publications were compared by Giustino *et al* [48].

C.2.1 Si-O-Si bond angle

Nakamura *et al* [15] explain the redshift of IR absorption by strained Si-O-Si bond angles in the interfacial layers. The local order for tetrahedral SiO_2 glass is shown in Figure C.2. The position of the transverse optical (TO) phonon peak of the Si-O-Si asymmetric stretching vibration depends on the Si-O-Si bond angle Θ. According to the Central Force Network Model by Sen and Thorpe [49] the TO anti-symmetric stretching frequency ω_{TO} can be approximated by

$$\omega_{TO}^2 = \frac{k}{m_O}(1 - \cos\Theta) \tag{C.1}$$

where Θ is the Si-O-Si inter-tetrahedral bond angle, k is the Si-O stretching force constant, and m_O is the mass of an oxygen atom. By replacing $(1 - \cos\Theta) = 2\sin^2(\Theta/2)$ and $\omega = 2\pi\nu$ we can rewrite

Equation C.1 as

$$\nu_{TO} = \nu_0 \sin(\Theta/2) \tag{C.2}$$

where $\nu_0 = 2\pi\sqrt{2k/m_O}$ is a constant. We can determine the value of ν_0=1134 cm^{-1} if we employ the literature values ν_{TO}=1078.5 cm^{-1} and $\Theta = 144°$ for completely relaxed bulk SiO$_2$ [47]. The peak position of the TO anti-symmetric stretching frequency is therefore a direct measure of the Si-O-Si bond angle. Changes in the bond angle which are related to a strained SiO$_2$ structure can be monitored.
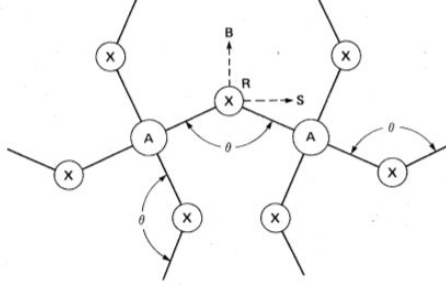

Figure C.2: Schematic diagram of local order for tetrahedral AX$_2$ glass [50]. Θ is the inter-tetrahedral angle. The symbols B, S and R indicate bending, stretching and rocking motions. Here A=Si and X=O for SiO$_2$ glass.

C.2.2 Si-O bond length

In a theoretical analysis by Giustino *et al* [48] the redshift of IR peaks in silicon oxide is explained by a difference of the Si-O bond length. The lengthening of the Si-O bond length can be attributed to the existence of Si^{+1}, Si^{+2}, Si^{+3} and Si^{+4} sub-oxides. A linear regression gives a redshift of 43 cm^{-1} for a bond length increase of 0.01 Å. The results are shown in Figure C.3.
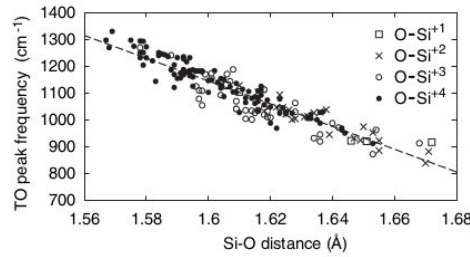

Figure C.3: Dependence of IR absorption on Si-O bond length [48]. The peak of the TO stretching frequency depends on the Si-O bond length. The Si-O bond length can further related to the existence of sub-oxides in the Si/SiO$_2$ interface.

Appendix D

Literature Review:

Silicon Oxidation by Ozone

This section is a review of various publications on silicon oxidation by ozone. The oxide growth properties will be discussed, followed by a summary of the advantages of ozone oxidation which have been reported. This section is included because the advantages of ozone oxidation have been carefully evaluated prior to the planning of the experiment.

D.1   Ozone generators

Conventional ozone generators produce ozone from oxygen using discharge processes (barrier discharge or corona discharge) or by UV-light radiation. The generated ozone concentration is < 5 % ozone in oxygen. There are various technologies to increase the ozone concentration: ozone jet generator [51], ozone silica gel [52], pulsed laser deposition [53], or a UV-assisted technology using a KrF lamp [54]. A nice overview over different high concentration ozone generators and their working principles can be found in a review by Fink *et al* [46]. Concentrations of 99 % ozone in oxygen have been achieved at a pressure of 10^3 Pa using an ozone jet generator [55]. Highly concentrated ozone enables fast oxidation rates at low temperatures. Layer-by-layer oxide growth at room temperature has been reported using 99 % ozone generated by ozone jet generator [56]. Extreme caution is necessary when working with highly concentration ozone. For our experiments we use a corona discharge ozone generator. The concentration of < 1 % ozone in oxygen provided by our generator (see calculation in 3.1.2) is enough to grow ultra-thin silicon oxide films at temperatures below 450 °C. Higher ozone concentrations would

be more dangerous.

D.2   Growth properties of ozone oxide

The growth properties of ozone were studied in detail in order to get a better understanding of the material properties and characteristics of ozone grown silicon oxide. The review by Fink *et al* [46] gives a nice overview over the growth properties. The key points are presented here.

D.2.1   Oxidation rate

An increased oxidation rate is observed when comparing oxidation in pure oxygen atmosphere with oxidation in ozone containing oxygen atmosphere. The relation between film thickness and oxidation time has been investigated. In most experimental studies the silicon oxide initially grew at a linear growth rate followed by a parabolic growth rate. The film thickness can be described by

$$x = At \tag{D.1}$$

$$x^2 = x_0^2 + Bt \tag{D.2}$$

where x is the oxide thickness, t is the oxidation time, x_0 is the thickness at which a transition from linear to parabolic growth occurs, and A and B are the linear and parabolic growth rate respectively. A linear growth rate usually indicates a surface or interface reaction-limited growth, while a parabolic growth rate suggests that the oxidation is governed by diffusion. Both growth rates are assumed to follow an Arrhenius behaviour. The temperature dependence of the growth rate can be described by

$$A = A_0 e^{-E_a^A/(kT)} \tag{D.3}$$

$$B = B_0 e^{-E_a^B/(kT)} \tag{D.4}$$

where E_a^A and E_a^B denote the activation energy [46]. The faster oxidation rate at higher temperature is explained by the Arrhenius behaviour of the growth rates.

D.2.2   Oxidation independent of crystalline orientation

Kameda *et al* reported that oxidation with ozone is independent of crystalline orientation [57]. They prepared a poly-crystalline sample from 15 x 15 mm^2 chips of a p-type Si(100) and a p-type Si(111)

wafer. An oxide film was grown on the sample in highly concentrated ozone. An electron microscopy image of the oxide film is shown in Figure D.2.2. The oxide film is homogeneous throughout the sample, which implies that the oxidation is independent of the crystalline orientation. This is a big advantage compared to conventional high-temperature oxygen oxidation methods where a strong variation for different crystalline orientations is observed.
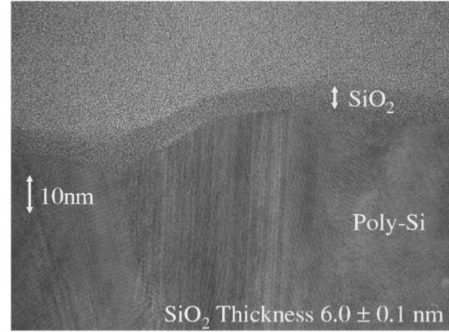

Figure D.1: Homogeneous oxide film on polycrystalline silicon [57]. Transmission electron microscopy image of cross section of poly-Si with SiO_2 film. A homogeneous 6.0 nm thick SiO_2 film was formed after ozone exposure for 30 min at 20 °C.

D.3   Silicon/silicon oxide interface

The Si/SiO_2 interface is described in the Theory Section 2.1.2. Several groups have reported on improved interface characteristics using ozone oxidation. A short summary of their results is given here.

D.3.1   HF etching rate of SiO2

The etching rate of silicon oxide in hydrofluoric acid (HF) is sensitive to the density, porosity, and composition of the oxide film and thus allows to probe the quality of the oxide. The HF etching rate has been studied and compared for ozone grown oxide and thermally grown oxide by Ichimura *et al* [58]. The oxide film of both samples was thinned down using hydrofluoric acid, and the silicon oxide thickness was measured using XPS. The results are shown in Figure D.2(a). Thermally grown oxide showed a change in etching rate for thinner oxide films, whereas the etching rate of the ozone grown oxide was independent of the film depth. The change in etching rate indicates that there is a structural or compositional change of the SiO_2 in thermally grown SiO_2 near the Si/SiO_2 interface. This change near the transition layer does not exist in ozone grown SiO_2, indicating that there are (almost) no transition layers.
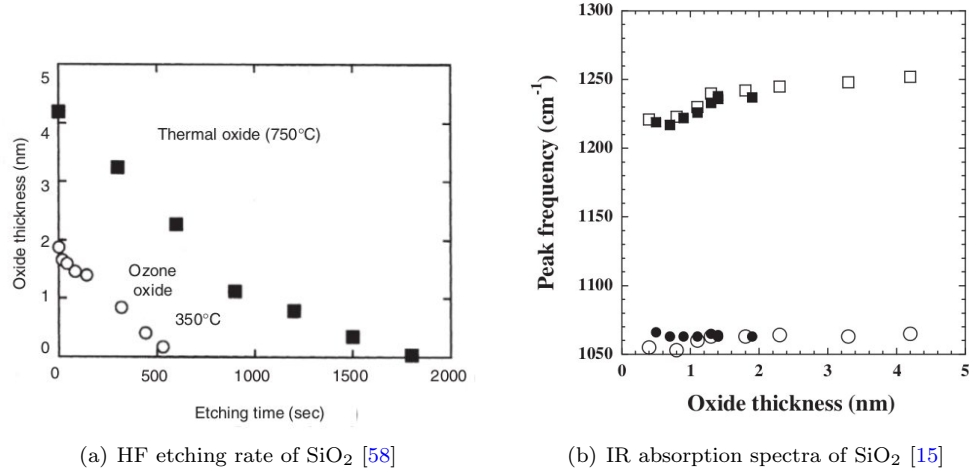
(a) HF etching rate of SiO$_2$ [58]   (b) IR absorption spectra of SiO$_2$ [15]

Figure D.2: Comparison of interface properties of ozone grown SiO$_2$ and thermally grown SiO$_2$. a) HF etching rate for ozone grown SiO$_2$ and thermally grown SiO$_2$. The etching rate for ozone grown remains constant, whereas the etching rate of thermally grown SiO$_2$ changes near the Si/SiO$_2$ interface. b) The TO phonon peak of SiO$_2$ is related to the Si-O-Si. For ozone grown SiO$_2$, the phonon peak is constant, indicating that there is (almost) no structural transition layer.

D.3.2   FT-IR measurement of the Si-O-Si bond angle

The FT-IR absorption spectrum is sensitive to the Si-O-Si bond angle as described in the Appendix Section C. The Si-O-Si bond angle has been studied and compared for ozone grown oxide and thermally grown oxide by Nakamura *et al* [15]. The study was based on the position of a transverse optical (TO) phonon peak of the Si-O-Si anti-symmetric stretching vibration ν_{TO} which is directly related to the Si-O-Si bond angle. A silicon sample with ozone grown SiO$_2$ was compared to a silicon sample with thermally grown SiO$_2$. Infrared absorption spectra of both samples were measured and then subtracted from an oxide-free silicon sample in order to analyze the pure SiO$_2$ film signal. The silicon oxide was then subsequently thinned down by etching with 0.1 % HF acid. After each etching step, the oxide thickness was measured using XPS and the infrared spectrum was measured using FT-IR. The position of the two dominant absorption peaks of SiO$_2$ was analyzed as shown in Figure D.2(b). The position of the TO phonon peak for ozone grown SiO$_2$ remained constant throughout the sample, whereas the position of the TO phonon peak for thermally grown SiO$_2$ changed below 1 nm thickness. This change in TO phonon peak for thermally grown SiO$_2$ is related to a change of Si-O-Si bond angle, and therefore explains the existence of a structural transition layer in thermally grown silicon oxide.

D.3.3   MEIS measurement of the Si/SiO₂ interface

Medium energy ion spectroscopy (MEIS) is a surface sensitive technique to measure both the structure and the composition of a surface. An ion beam is focused on the sample the resulting particles are analyzed. The incoming ion beam can induce several events at the surface, including electron or photon emission, electron transfer (ion-to-surface or surface-to-ion), scattering, absorption and sputtering. The composition and the bond angle of the neighboring atoms can be directly extracted from the MEIS data. Measurements can be done with a depth resolution of several atomic layers.

Strain measurement using MEIS

Chang *et al* compared MEIS measurements of thermally grown SiO_2 and ozone grown SiO_2 [28]. They used p-type silicon wafer with an oxide thicknesses of 4 nm. The thermal oxide was grown at 800 °C, while the ozone oxide was grown in 3 % ozone in oxygen at 600 °C. Figure D.3 shows the shift in bond angle as a function energy for the ozone oxide and thermal oxide. A higher energy corresponds to a higher depth and therefore probes the region near the Si/SiO_2 interface. It can clearly be seen that the bond angle changes only in the thermal oxide sample for higher energies. The change in bond angle for the thermal oxide can be explained by a compressive strain of the Si lattices at the interface. The constant position of the ozone oxide bond angle implies that there is no compressive strain at the interface.
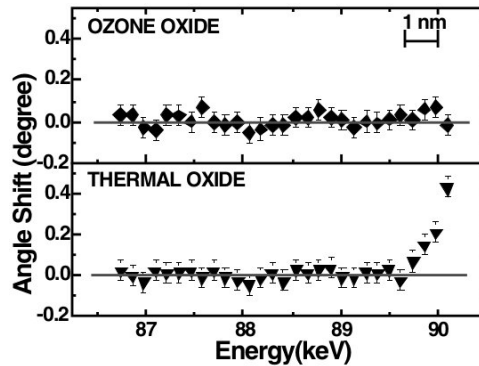

Figure D.3: Change of bond angle as a function of energy [28]. A higher energy is related to a higher sampling depth. When approaching the Si/SiO_2 interface, the bond angle of ozone oxide remains constant, while the bond angle of the thermal oxide is shifted.

D.4   Simulation of ozone oxide growth

The growth characteristics for ozone oxidation were studied by Fink *et al* using density-functional theory [59]. All possible reaction products were studied and their energetic stability was compared. Fink *et al* found that the initial oxidation steps of ozone oxidation are distinct from oxidation using other oxygen species. Ozone exhibited a very high reaction probability, corresponding to an initial sticking probability close to unity. Two dominant reaction pathways were observed, where O_3 dissociatively adsorbed either into a single O adatom and gas-phase O_2 (partial dissociation) or into three O adatoms (complete dissociation). The partial dissociation is the preferred reaction pathway, since the complete dissociation is sterically more challenging. Oxygen however always needs to dissociate completely when reacting with the silicon surface which proceed only via a very narrow dissociation pathway. This results explains why ozone oxidation is much faster than oxygen oxidation. We are interested in the oxidation behaviour of a partly oxidized silicon surface because a thin native silicon oxide layer begins to grow instantaneously on a pure silicon surface in air. A molecular dynamics simulation by Fink *et al* [46] is shown in Figure D.4. Ozone preferentially reacts with surface Si atoms which have a lower oxidation state. This leads to a uniform oxidation which could explain the better interface quality as explained in 2.1.2. After the first oxide layers have been built, the later oxidation is controlled by diffusion of O atoms. Here the oxidation rate of ozone is faster because the formation of an adsorbed oxygen atom O(a) at the surface is much easier for ozone $O_3 \rightarrow O_2(g) + O(a)$ than for oxygen.
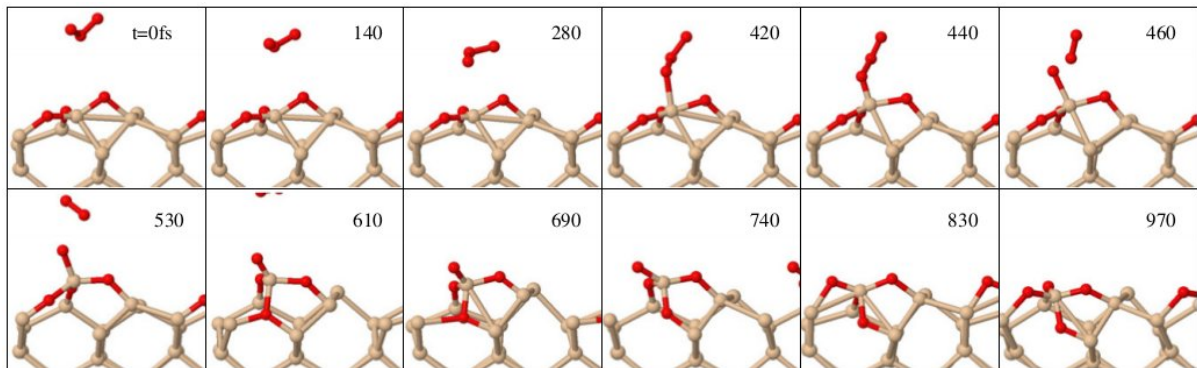

Figure D.4: Molecular dynamics trajectory for O_3 approaching the partially oxidized Si(100) surface [46]. An O_3 molecule can bring one of its terminal O atoms into the vicinity of the Si^{3+} site, which initiates the adsorption of a single O adatom and the subsequent migration of an O atom from the back bond into the subsurface site.

Appendix E

Erklärung zur Wissenschaftlichen Redlichkeit